Izvestiya, Physics of the Solid Earth, Vol. 38, No. 10, 2002, pp. 816–845. Translated from Fizika Zemli, No. 10, 2002, pp. 23–53.
Original Russian Text Copyright © 2002 by Vanyan, Berdichevsky, Pushkarev, Romanyuk.
English Translation Copyright © 2002 by MAIK "Nauka/Interperiodica" (Russia).

A Geoelectric Model of the Cascadia Subduction Zone

L. L. Vanyan[1†], M. N. Berdichevsky[2], P. Yu. Pushkarev[2], and T. V. Romanyuk[3]

[1] *Shirshov Institute of Oceanology, Russian Academy of Sciences, Nakhimovskii pr. 36, Moscow, 117218 Russia*

[2] *Moscow State University, Vorob'evy gory, Moscow, 119899 Russia*

[3] *Schmidt United Institute of Physics of the Earth, Russian Academy of Sciences, Bol'shaya Gruzinskaya ul. 10, Moscow, 123995 Russia*

Received February 15, 2002

Abstract—Results of the EMSLAB geoelectric experiment aimed at studying the Cascadia subduction zone are discussed. A 2-D interpretation of magnetic variation and magnetotelluric data was conducted in a hypothesis-testing mode. Three hypotheses were examined: (1) fluid saturation of the lower continental crust and the absence of continental asthenosphere; (2) fluid saturation of the lower continental crust and development of a continental asthenosphere; and (3) a subvertical zone of melting penetrating the continental lithosphere. The first stage of the interpretation involved experiments on smoothed inversion with the REBOCC program. These experiments showed that, under the complex conditions of the Cascadia subduction, simultaneous inversion of TE and TM modes yields an intricate, geophysically meaningless alternation of conducting and nonconducting zones with a poor minimization of the misfit. The most interesting result was obtained from the autonomous inversion of the TE mode (tippers and longitudinal impedance phases). The resistivity section comprises three subvertical zones reaching mantle depths: the oceanic (conducting), coastal (nonconducting), and Cascadia (conducting) zones. Notwithstanding its simplified nature, this result outlines the development of oceanic and continental asthenosphere. The second stage of the interpretation employed the II2DC and IGFMT2D programs using models with a fixed geometry of blocks. The inversion was conducted on a relatively detailed grid allowing, during the misfit minimization, a free choice of crustal and mantle structures corresponding to various hypotheses on the structure of the Cascadia subduction zone. The interpretation algorithm consisted of a sequence of partial target inversions taking into account variations in the sensitivity and robustness of components of the TE and TM modes. In our opinion, this type of algorithm yields the most reliable and detailed results under conditions of the Cascadia subduction. The interpretation included four successive levels: (1) inversion of tippers; (2) inversion of longitudinal impedance phases; (3) inversion of transverse apparent resistivities and transverse impedance phases; and (4) generalization and geological interpretation. Tippers played the main role, because with decreasing frequency they become free from the distorting effect of near-surface heterogeneities. A new geoelectric model of the Cascadia subduction zone was constructed. Its main distinctive features are as follows: (1) at depths of up to 40 km, a conducting upper part of the downgoing plate containing fluids of oceanic and possibly dehydration origin is clearly identifiable; and (2) the continental section contains a conducting crustal layer and a conducting asthenosphere that are connected by a subvertical conducting zone of wet melting confined to the High Cascade volcanic arc. The reliability of the model is confirmed by tests. The model agrees well with the modern concepts of the Cascadia subduction zone.

1. INTRODUCTION

In 1978, on the initiative of L.L. Vanyan, a global geoelectric project was organized under the auspices of the International Association of Geomagnetism and Aeronomy (IAGA) with the aim of studying deep conductivity characterizing melting processes in the asthenosphere. Work on this project, named ELAS (**EL**ectrical Conductivity of the **AS**thenosphere), was conducted throughout the world, and the objectives of the project were extended. Deep geoelectrics began to be applied to the investigation of the conductivity in the lithosphere and asthenosphere in order to elucidate the fluid regime and rheology of the Earth's interior [Vanyan, 1997]. The ELAS project brought geoelectrics to the forefront of modern geodynamics.

One of the most important events in the history of the ELAS project was the EMSLAB (**E**lectro**M**agnetic **S**tudy of the **L**ithosphere and **A**sthenosphere **B**eneath the Juan de Fuca plate) experiment conducted from 1985 to 1988 by US, Canadian, and Mexican geophysicists on the Pacific coast of North America in the Cascadia subduction zone (where the Juan de Fuca microplate subducts under the northwestern continental margin).

Figure 1 shows the network of electromagnetic observations performed within the framework of the EMSLAB experiment [Wannamaker *et al.*, 1989a].

† Deceased.

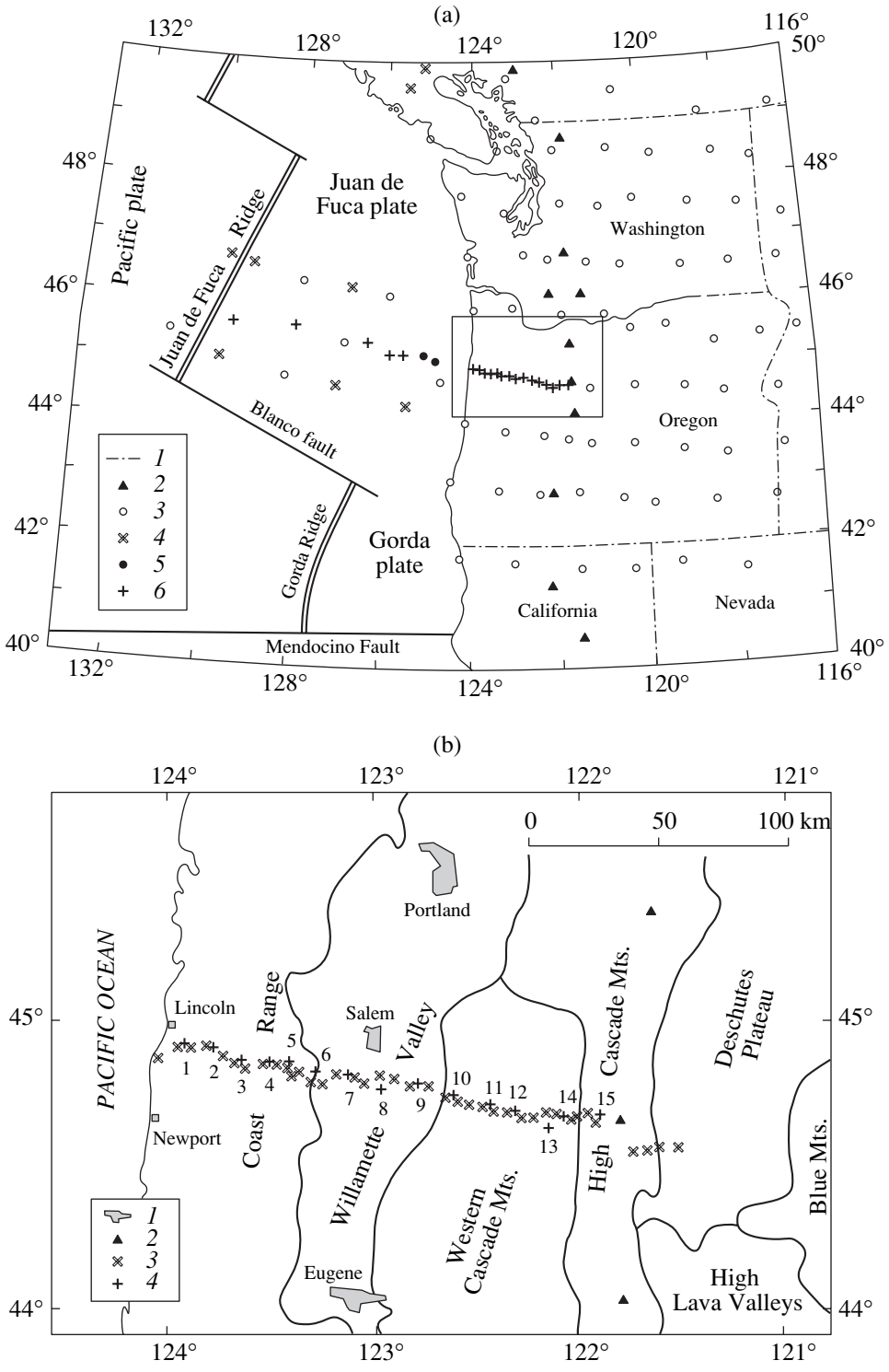

Fig. 1. Electromagnetic sounding network in the EMSLAB experiment [Wannamaker *et al.*, 1989a]. (a) General scheme: (*1*) state boundaries; (*2*) areal survey MV sounding; (*3*) areal survey MT sounding; (*4*) MV sounding on the Lincoln line; (*5*) MT sounding on the Lincoln line. (b) Schematic map showing continental magnetotelluric sounding sites: (*1*) towns; (*2*) volcanoes; (*3*) MT sounding; (*4*) deep MT sounding.

Almost the entire Juan de Fuca plate is covered by magnetic variation (MV) observations with a spacing of 50 to 100 km. Magnetotelluric soundings (MTS) were performed on an E–W profile near the town of Lincoln. This profile was named the Lincoln line. Spacings of magnetotelluric (MT) and MV observations on the Lin-

coln line were about 5 km (39 MTS sites) in a period range of 0.01–500 s and 10 km (15 deep MTS sites) in a period range of 50–10000 s.

Researchers involved in the EMSLAB experiment hoped to obtain new constraints on the structure and state of the crust and upper mantle in the subduction zone. However, the capabilities of computational geoelectrics were limited at that time.

The first geoelectric models of the Cascadia subduction zone were constructed either by means of the Backus–Gilbert smoothing method [Jiracek *et al.*, 1989] or manually, by the trial-and-error approach [Wannamaker *et al.*, 1989b; Vanyan *et al.*, 1988]. They clearly showed that magnetotellurics can serve as a powerful tool for studying the subduction zone. Presently, we recall these models with an understanding of the important role that they played in the history of deep geoelectric research. The 1990s were marked by a rapid development of computational geoelectrics. The creation of programs for the computation of the electromagnetic field in complex media and for the inversion of MT and MV data opened the way toward the improvement and partial revision of the EMSLAB results [Zhdanov and Spichak, 1992; Berdichevsky *et al.*, 1992; Varentsov *et al.*, 1996]. In this paper, we revert to the EMSLAB experiment and apply a new interpretation technology based on the priority of MV sounding. The implementation of this technology was made possible by recent achievements of computational geoelectrics [Siripunvaraporn and Egbert, 2000; Varentsov, 1999; Novozhinskii and Pushkarev, 2001]. Based on this approach, we construct a new geoelectric model of the Cascadia subduction zone that fills some gaps in the current theories on the subduction of the Juan de Fuca plate.

2. BRIEF TECTONIC AND GEOLOGICAL DESCRIPTION OF THE CASCADIA SUBDUCTION ZONE

The study region forms part of the tectonically active Pacific orogenic belt, characterized by intense Tertiary and Quaternary volcanism. The continental section is dominated by volcanic rocks and structures: lava plateaus, volcanic cones, and ridges produced by accumulation or deformation of eruptive rocks. The origin of the main geological structures of the region is due to subduction and its accompanying volcanism [Khain *et al.*, 1988; Khain and Lomize, 1995]. All these structures extend N–S for up to 300–500 km. The N–S (x) and E–W (y) directions can be regarded as the major tectonic directions of the region, corresponding to the longitudinal ($\parallel$) and transverse ($\perp$) components of the impedance tensor.

The Juan de Fuca spreading ridge, giving rise to the Juan de Fuca plate, is located at a short distance from the coast (about 500 km); therefore, the age of the subducting plate is young (less than 10 Ma). The present-day subduction rate is relatively slow, amounting to about 4 cm/yr.

The following structures are traceable in the eastward direction from the Juan de Fuca ridge: (1) the abyssal basin of the Juan de Fuca plate; (2) the continental slope consisting of compacted sediments of the accretionary prism; (3) the shelf covered by loose sediments; (4) the Coast Range composed of volcanic–sedimentary rocks of the Siletz complex; (5) the gently dipping Willamette Valley filled with a thick sequence of sediments and basaltic intrusions; (6) the Western (older) and (7) High (younger) Cascade mountains composed of volcanic and volcanic–sedimentary rocks typical of present-day active volcanic arcs; and (8) the lava-covered Deschutes Plateau.

The oceanic crust within the abyssal basin of the Juan de Fuca plate has a structure typical of the Pacific and other oceans. It comprises three layers: (1) a sedimentary layer 1 to 2 km thick; (2) a 1.5- to 2-km-thick layer of basalts (pillow lavas) and basaltic flows with dolerite dikes; and (3) a layer of fully crystalline igneous rocks (gabbro and ultramafic varieties) 3 to 4 km thick.

The Cascade Range includes high peaks and sharply defined mountain crests. The highest peaks are volcanic cones developed on the ancient basement. The mountain structures are composed of Oligocene–Pliocene volcanics represented by lava flows and significant amounts of breccias, tuffs, and mudflow deposits. The structure of the Cascade Range is complicated by the emplacement of intrusive massifs.

The more easterly plateau is also dominated by volcanics with prevailing Pliocene and Pleistocene lavas.

3. GEOPHYSICAL RESEARCH IN THE CASCADIA SUBDUCTION ZONE

Figure 2 presents a schematic map of the Cascadia subduction zone, reflecting the main features of contemporary tectonic processes: crustal seismicity, volcanism, and formation of the accretionary complex. Earthquake sources concentrate in the northern and southern parts of the subduction zone, whereas the subduction is aseismic in its central part, in the state of Oregon: the Benioff zone is reliably traceable only within the states of Washington and California [Kelly and Crosson, 1984]. According to seismological evidence, the oceanic plate subducts at a low angle in these areas, with its dip gradually increasing to 45°. In the Oregon area, the plate also starts subducting at a low angle, but seismic tomography data indicate that, at depths of about 40 to 80 km, it is sharply curved and then descends at an angle of about 70° [Weaver and Michaelson, 1985].

The most comprehensive seismic model of the central Cascadia subduction zone developed by Trehu *et al.* [1994] is based on reflection data and natural seismicity observations. Figure 3 shows the velocity structure

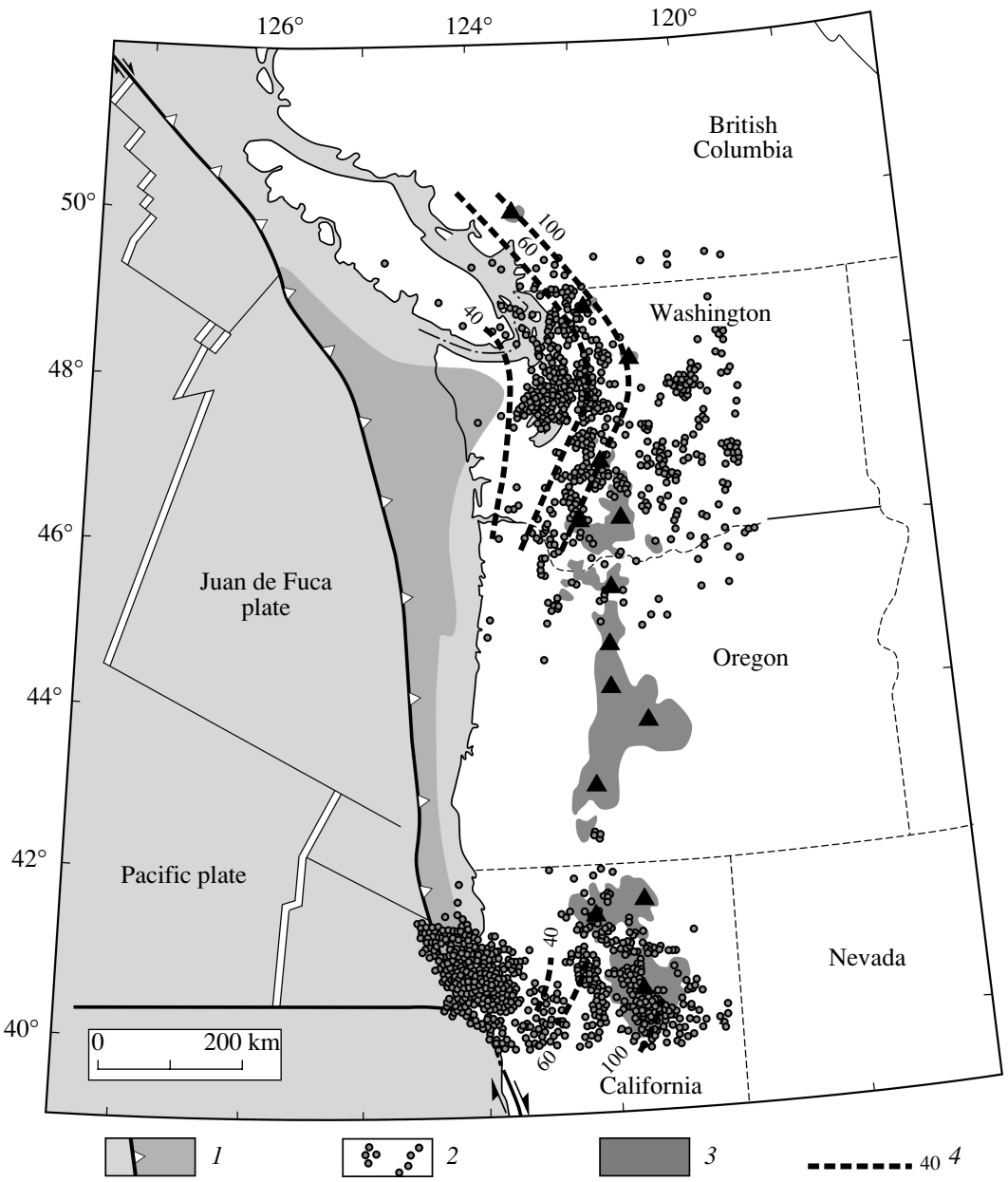

Fig. 2. Evidence of recent tectonic processes [Romanyuk *et al.*, 2001b]: (*1*) accretionary complex; (*2*) crustal seismicity; (*3*) Quaternary volcanic rocks; (*4*) depth to the Benioff zone (in km).

along an E–W profile near the Lincoln line. The downgoing slab with velocities increasing down the dip from 6.5 to 8 km/s is clearly recognizable. The continental part of the seismic section is characterized by a more or less gently dipping bedding, with a monotonic increase in the velocities from 5 km/s at depths of 1–2 km to 7 km/s at depths of about 20 km. No *P* wave velocity inversion was discovered within the crust.

According to seismic refraction data, the near-surface *P* wave velocities range from 2.9 to 5.2 km/s; the upper and middle crust at depths of 3 to 30 km is characterized by velocities of 6.1 to 6.5 km/s. Beneath the High Cascades, the lower crust at a depth of 45 km has a velocity of about 7 km/s [Leaver *et al.*, 1984]; the Moho is fixed at a depth of 45 km. Importantly, a low-velocity layer was identified, although not very reliably, in the middle crust [Stanley *et al.*, 1989].

Gravity data were used by Romanyuk *et al.* [2001a] to construct a 2-D density model of the Cascadia subduction zone along a profile crossing central Oregon (Fig. 4). The oceanic crust has densities of 1.90–2.45 g/cm^3 (sediments), 2.79 g/cm^3 (basalts and dolerites), and 3 g/cm^3 (gabbros and ultramafic rocks). The oceanic mantle to a depth of 40 km has a density of 3.33 g/cm^3 (lithosphere). In a depth range of 40–140 km, its density is 3.3 g/cm^3 (asthenosphere).

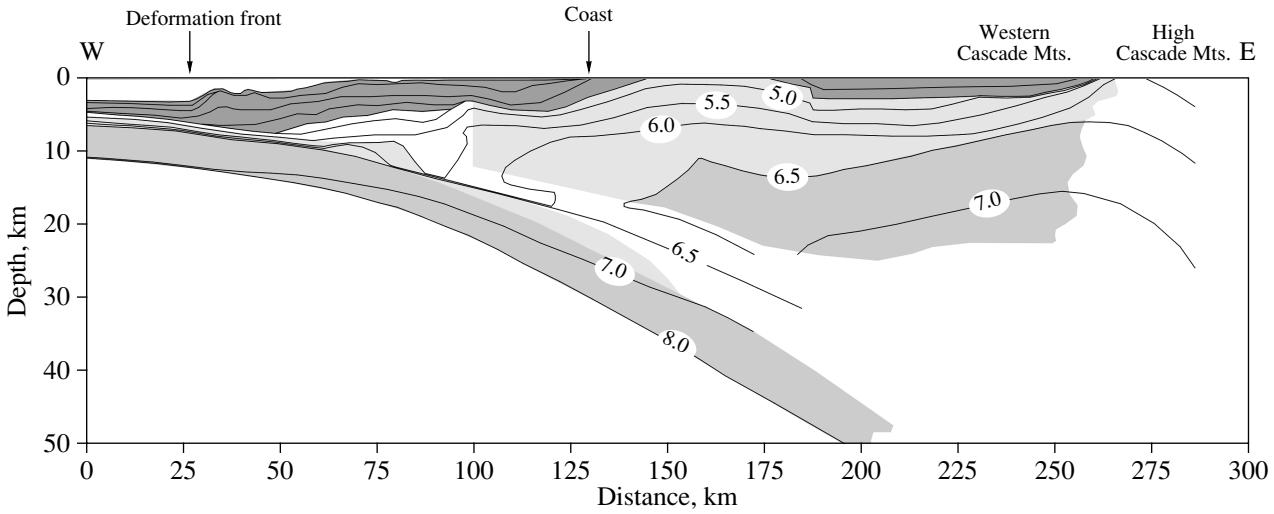

Fig. 3. Deep seismic section along an E–W profile close to the Lincoln line [Trehu *et al.*, 1994]. Numbers indicate *P* wave velocities (in km/s).

The underlying rocks have a density of 3.32 g/cm^3. The densities of the oceanic lithosphere and asthenosphere increase as they subduct under the continent.

Data of numerous measurements of the heat flow and temperature gradient are available for the Cascadia subduction zone. Near the Coast Range and the Willamette Valley, the heat flow amounts to 40 mW/m^2 and the temperature gradient is about 30°C/km. They increase in the Western Cascades and reach 105 mW/m^2 and 65°C/km in the High Cascades. This area contains numerous hot springs. The Cascades heat flow maximum is attributed to the influence of an extensive magma chamber at depths of about 10 to 20 km [Stanley, 1984; Ramires, 1988; Blackwell *et al.*, 1989]. On the other hand, Ingebritsen *et al.* [1989] suggested that heat rises from great depths through a relatively narrow zone.

Figure 5 shows a predictive geothermal and petrological model of the Cascadia subduction zone (hereafter referred to simply as CASCADIA), generalizing current ideas of the structure of the region and its fluid regime [Romanyuk *et al.*, 2001b]. The prediction is based on the heat flow, estimated depths of the Curie isotherm (~500°C), petrological analysis of magmas, and some other data. The continental crust above the downgoing Juan de Fuca plate in the near-shore area is characterized by lower temperatures. A subvertical zone of higher temperatures reaching the melting point of wet peridotite at the Moho (~900°C) has been localized beneath the High Cascades.

The release of fluids in the upper part of the slab can be due to several mechanisms. First, free water of micropores and microfractures is released under the action of increasing lithostatic pressure at depths of up to 30 km. Then, at depths of 30 to 50 km, where the temperature exceeds 400°C, dehydration of minerals such as talc, serpentine, and chlorite starts. Finally, basalt is transformed into eclogite at depths greater than 75 km, and amphibolite exsolution can take place at depths exceeding 90 km. All these processes are accompanied by release of fluids. Supposedly, fluids released at shallow depths migrate through the contact zone between the subducting slab and the continental plate. At greater depths, fluids can be absorbed by mantle peridotites (serpentinization) at lower temperatures and disturb phase equilibria at higher temperatures, giving rise to wet melting. Melts migrate upward to the Earth's surface, resulting in the formation of a volcanic arc.

In conclusion, we note the results of bottom frequency sounding on the Pacific Plate [Vanyan, 1997]. The upper part of the oceanic crust consisting of sediments and basaltic pillow lavas is characterized by a higher porosity and has a resistivity of 3–10 Ω m. Below, the resistivity markedly increases, reaching at least 10000 Ω m.

Such is the *a priori* geological and geophysical information on the basis of which we interpret geoelectric data obtained on the Lincoln line.

4. MT AND MV SOUNDINGS ON THE OCEAN COAST (ANALYSIS OF 2-D MODELS)

The resistivity contrast on the ocean coast, reaching three and even four orders of magnitude, causes a strong MT anomaly referred to as the "coast effect." This anomaly has galvanic and inductive components.

The galvanic (conductive) anomaly arises if an electric current flows perpendicular to the shoreline (the TM mode of the MT field). The shoreward oceanic electric current branches. One branch flows into the sedimentary cover. Sediments capture the oceanic cur-

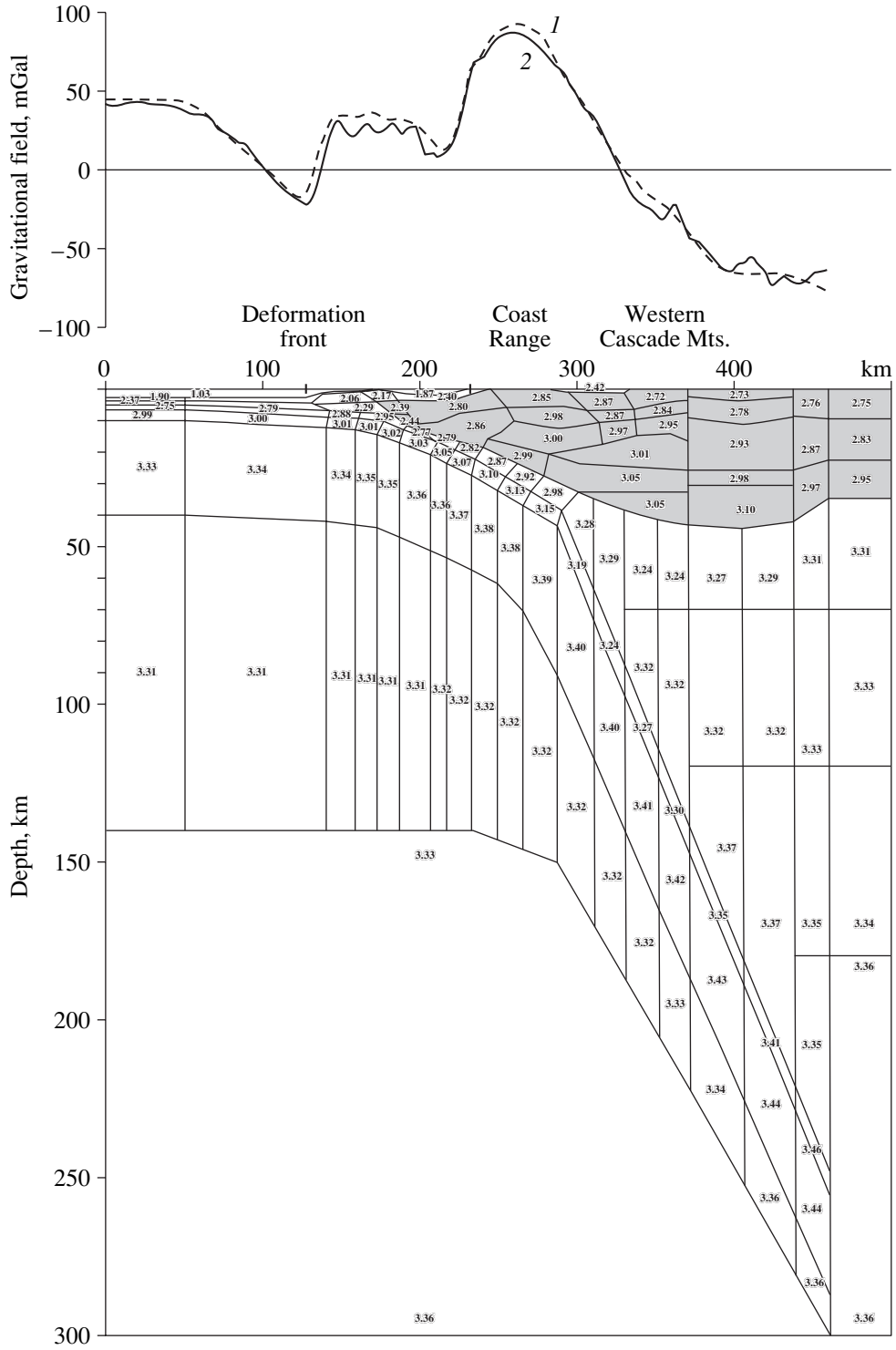

Fig. 4. Density model along the E–W profile crossing central Oregon [Romanyuk *et al.*, 2001a]: (*1*) model; (*2*) observations. Numbers indicate densities (in g/cm^3).

rent and channel it far from the coast, with its slow leakage into the crystalline basement and deep conducting zones. This phenomenon can be referred to as a continental trap effect. The size of the continental trap is on the order of the normalization distance $\sqrt{S_1 R_2}$, where $S_1 = h_1/\rho_1$ is the average conductance of the sedimentary cover and $R_2 = h_2\rho_2$ is the average resistance of the high-resistivity crust that separates the sedimentary cover from the deep conducting zone. Another branch of the oceanic electric current bypasses the continental

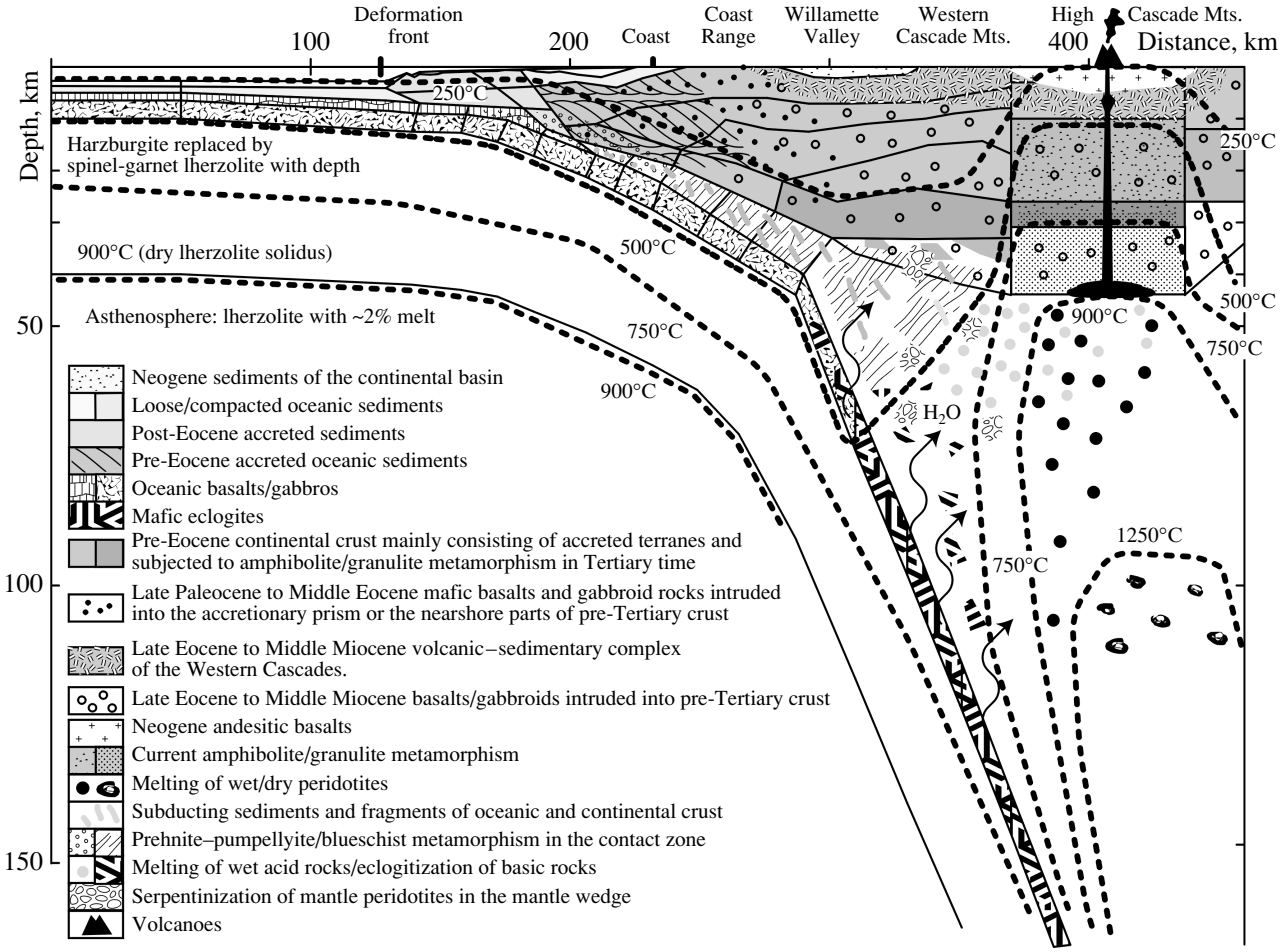

Fig. 5. Predictive geothermal and petrological model CASCADIA along the E–W profile crossing central Oregon [Romanyuk *et al.*, 2001b].

trap. The current leaks into the ocean floor and is distributed among continental deep conducting zones. The relative proportions of the currents flowing into the continental trap and penetrating deep conductors control the amount of low-frequency near-surface distortion of transverse MT curves and their sensitivity to crustal and mantle conductivity anomalies.

The inductive anomaly is associated with the electric current parallel to the coast (the TE mode of the MT field). It is caused by the inductive interaction between oceanic and continental longitudinal electric currents and can be referred to as a horizontal skin effect (at high frequencies, the longitudinal excessive current concentrates in the coastal zone). Inductive distortions of longitudinal MT curves are observed near the shore and decay at distances of the same order as the depth to the well-conducting mantle. The asymmetry of longitudinal currents generates the vertical component of the magnetic field, which can exceed its horizontal component in the coastal zone.

For illustration, we turn to the work of Berdichevsky *et al.* [1992] and address MTS curves calculated in terms of 2-D models A and S; geologically, these models are substantially different (Fig. 6). The right-hand (continental) part of model A involves a thick conductor, encompassing the crust and upper mantle (supposedly, an active tectonic zone). In the same depth range, model S contains a thin crustal layer, encountered in stable tectonic zones.

Comparing models A and S, we see that, on the continental profile, the transverse apparent resistivity curves $\rho_A^{\perp}$ and $\rho_S^{\perp}$ obtained from these different models are similar, whereas the longitudinal apparent resistivity curves $\rho_A^{\parallel}$ and $\rho_S^{\parallel}$ differ. In an 85-km-wide alongshore band, the $\rho_A^{\perp}$ and $\rho_S^{\perp}$ curves virtually coincide (they differ by no more than 3% throughout the period range considered), whereas the divergence between the $\rho_A^{\parallel}$ and $\rho_S^{\parallel}$ curves reaches 300%.

The behavior of the apparent resistivity curves is characteristic. Near the coast, the high-frequency branches of the transverse $\rho_A^{\perp}$ and $\rho_S^{\perp}$ curves coincide

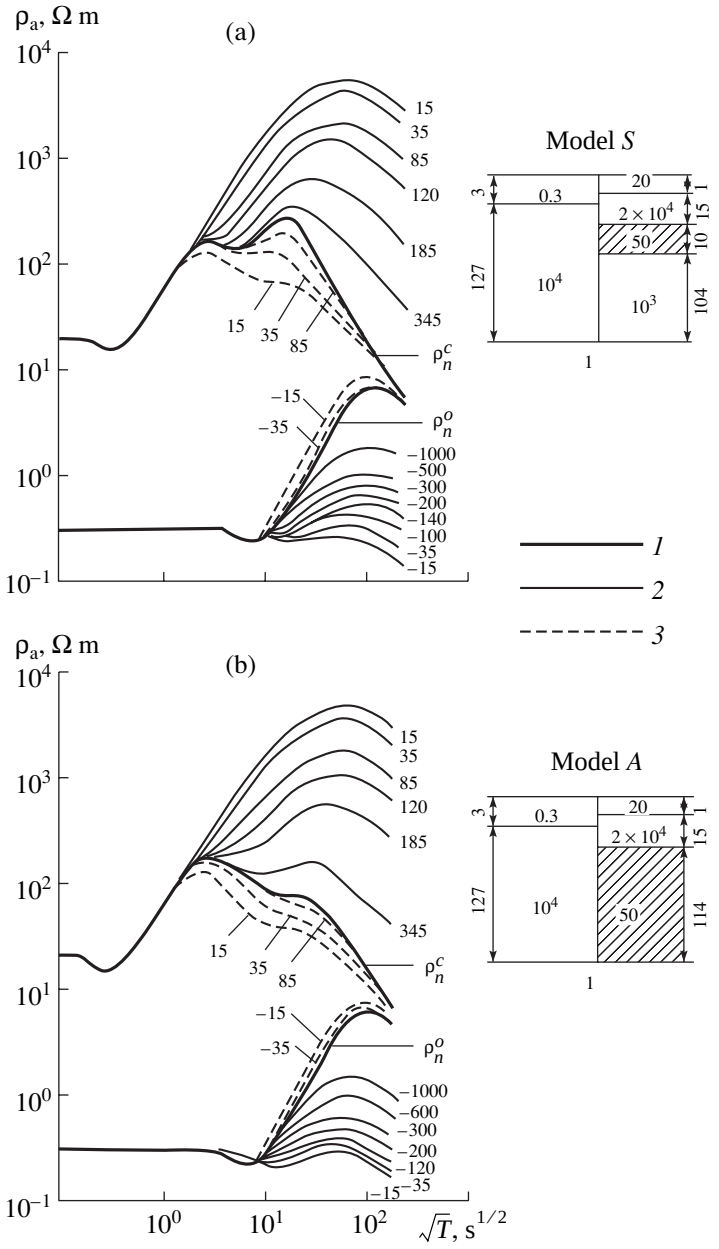

Fig. 6. Apparent resistivity curves in models involving a stable (S) and active (A) tectonic zones [Berdichevsky *et al.*, 1992]: (*1*) normalized curves ρ_n^c (continent) and ρ_n^o (ocean); (*2*) transverse $\rho^\perp$ curves; (*3*) longitudinal $\rho^\parallel$ curves. The parameter of the curves is the distance to the coast (in km). Resistivities (Ω m) and thicknesses (km) of layers are shown in the model sections: (a) model *S*; (b) model *A*.

with the normal curve ρ_n^c. However, with decreasing frequency, the $\rho_A^\perp$ and $\rho_S^\perp$ curves depart from the ρ_n^c curve: the ascending branches are elongated, and the descending branches shift upward by 2.5 decades. No evidence of a crustal or crust–mantle conducting layer is available there. With increasing distance from the ocean, the shape of the $\rho_A^\perp$ and $\rho_S^\perp$ curves slowly changes, with the appearance of gentle inflections followed by minimums; finally, at a distance of about 700 km (six normalization distances), the $\rho_A^\perp$ and $\rho_S^\perp$ curves merge with the normal curve ρ_n^c. The behavior of the transverse apparent resistivity curves can be easily attributed to the continental trap effect. The situation with the longitudinal $\rho_A^\parallel$ and $\rho_S^\parallel$ curves is different. Their behavior is governed by the inductive effect. Even in the coastal zone, they have distinct inflections

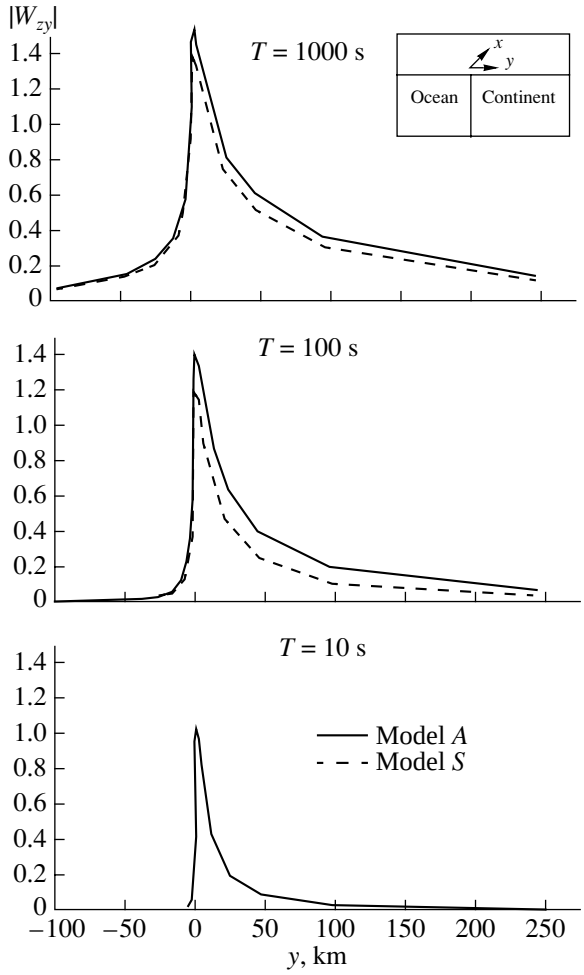

Fig. 7. Tipper modulus curves in the models involving stable (*S*) and active (*A*) tectonic zones. Parameters of the models S and A are the same as in Fig. 6.

and minimums indicating the presence of a crustal or crust–mantle conducting layer. At a distance of about 100 km from the coast, the $\rho_A^{\parallel}$ and $\rho_S^{\parallel}$ curves merge with the normal curve ρ_n^c.

To continue our analysis of the TE mode, we examine the behavior of the tipper $|W_{zy}|$. Figure 7 shows the $|W_{zy}|$ curves. The coast effect produces an extensive $|W_{zy}|$ anomaly extending at low frequencies for about 100 km in the ocean and 300 km on the continent. At periods of 100 and 1000 s, models A and S yield distinctly different results even in the coastal zone.

Evidently, the TE mode on the coast (longitudinal magnetotelluric curves and tipper) is more sensitive to mantle conducting zones compared to the TM mode (transverse MT curves).

This statement, derived from the analysis of simple models, needs further elaboration with reference to the subduction zone. Figure 8 presents a block model of the subduction zone involving the following components:

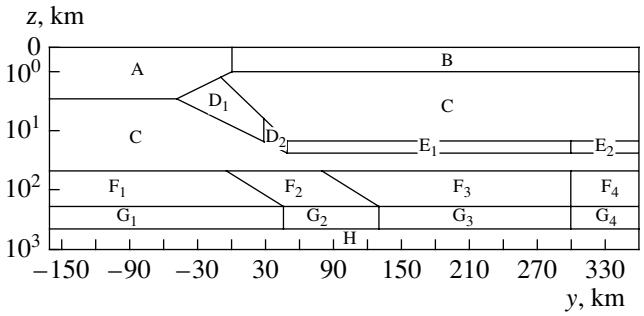

Fig. 8. Block model of the subduction zone.

(1) *A*, ocean; (2) *B*, continental sedimentary cover; (3) C, lithosphere; (4) D_1 and D_2, upper part of the slab; (5) E_1 and E_2, continental crustal conducting layer; (6) F_1, oceanic asthenosphere; (7) F_2, F_3, and F_4, continental asthenosphere; (8) G_1, oceanic mantle; (9) G_2, G_3, and G_4, continental mantle; and (10) *H*, mantle. Varying the resistivities of blocks D_1, D_2, E_1, E_2, F_2, F_3, F_4, G_2, G_3, and G_4, we construct a model series enabling the estimation of the sensitivity of longitudinal and transverse apparent resistivities to the subducting plate, continental crustal conductors, and continental asthenosphere. The basic model has a continental section without crustal conductors and conducting asthenosphere. It is successively complicated by introducing the following units into the continental section: (1) a crustal conducting layer (either of infinite extent or 300 km wide); (2) a downgoing conducting plate either connected or unconnected with the crustal conducting layer; and (3) a conducting asthenosphere (either of infinite extent or 300 km wide) connected or unconnected with the crustal conducting layer. The model series comprises the following models:

model I: a crustal conducting layer, a downgoing conducting plate, and a conducting asthenosphere are absent;

model II: a crustal conducting layer of infinite extent is introduced into model I;

model III: a crustal conducting layer of a finite extent is introduced into model I;

model IV: a downgoing conducting slab is introduced into model II;

model V: a downgoing conducting slab is introduced into model III;

model VI: the downgoing conducting slab in model IV is connected with a crustal conducting layer of infinite extent;

model VII: the downgoing conducting slab in model V is connected with a 300-km-wide crustal conducting layer;

model VIII: a continental asthenosphere of infinite extent is introduced into model VI;

model IX: a 300-km-wide continental asthenosphere of infinite extent is introduced into model VI;

Table 1. Parameters of the models characterizing the MTS sensitivity (resistivities of blocks in units of Ω m are given)

Model	A	B	C	D_1	D_2	E_1	E_2	F_1	F_2	F_3	F_4	G_1	G_2	G_3	G_4	H
I	0.3	10	10^4	10^4	10^4	10^4	10^4	30	10^3	10^3	10^3	10	10^2	10^2	10^2	3
II	0.3	10	10^4	10^4	10^4	10	10	30	10^3	10^3	10^3	10	10^2	10^2	10^2	3
III	0.3	10	10^4	10^4	10^4	10	10^4	30	10^3	10^3	10^3	10	10^2	10^2	10^2	3
IV	0.3	10	10^4	10	10^4	10	10	30	10^3	10^3	10^3	10	10^2	10^2	10^2	3
V	0.3	10	10^4	10	10^4	10	10^4	30	10^3	10^3	10^3	10	10^2	10^2	10^2	3
VI	0.3	10	10^4	10	10	10	10	30	10^3	10^3	10^3	10	10^2	10^2	10^2	3
VII	0.3	10	10^4	10	10	10	10^4	30	10^3	10^3	10^3	10	10^2	10^2	10^2	3
VIII	0.3	10	10^4	10	10	10	10	30	10^3	30	30	10	10^2	10	10	3
IX	0.3	10	10^4	10	10	10	10	30	10^3	30	10^3	10	10^2	10	10^2	3
X	0.3	10	10^4	10	10	10	10	30	30	30	30	10	10	10	10	3
XI	0.3	10	10^4	10	10	10	10	30	30	30	10^3	10	10	10	10^2	3
XII	0.3	10	10^4	10	10	10	10^4	30	10^3	30	30	10	10^2	10	10	3
XIII	0.3	10	10^4	10	10	10	10^4	30	30	30	30	10	10	10	10	3
XIV	0.3	10	10^4	10	10	10	10^4	30	10^3	30	10^3	10	10^2	10	10^2	3
XV	0.3	10	10^4	10	10	10	10^4	30	30	30	10^3	10	10	10	10^2	3

model X: the continental asthenosphere of infinite extent in model VIII is connected with the oceanic asthenosphere;

model XI: the 300-km-wide continental asthenosphere in model IX is connected with the oceanic asthenosphere;

model XII: a continental asthenosphere of infinite extent is introduced into model VII;

model XIII: the continental asthenosphere of infinite extent in model XII is connected with the oceanic asthenosphere;

model XIV: a 300-km-wide continental asthenosphere is introduced into model VII; and

model XV: the 300-km-wide continental asthenosphere in model XIV is connected with the oceanic asthenosphere.

The parameters of these models are summarized in Table 1.

The MTS sensitivity $\eta(U)$ to the element U of a given model is estimated in three zones of the continental profile Y: the coastal zone ΔY_1 ($0 < y < 40$ km), the central zone ΔY_2 ($40 < y < 130$ km), and the far-field zone ΔY_3 ($130 < y < 300$ km). The estimates given in Tables 2 and 3 were calculated by the formula

$$\eta(U) = \max_{T,\,Y}\left|\frac{\rho_a(L)-\rho_a(\mathrm{M})}{\min[\rho_a(L),\rho_a(\mathrm{M})]}\right|100\%,$$

where M is a model in which the element U is absent and L is the same model including the element U. Analysis of the results leads to the following evident conclusions.

(1) The crustal conducting layer is best expressed in the TE mode. The sensitivities of the longitudinal and transverse apparent resistivities $\rho^{\parallel}$ and $\rho^{\perp}$ to the crustal conductor of infinite and finite extent in the coastal and central zones differ by nearly one order of magnitude.

(2) If the subducting oceanic plate is not connected with the crustal conducting layer, it has a distinct signature only in the coastal curves $\rho^{\parallel}$. The conductive connection of the plate with the crustal conducting layer is best resolved in the TM mode.

(3) The conducting continental asthenosphere is better resolved in the TE mode as compared with the TM mode. The sensitivities of the longitudinal and transverse apparent resistivities $\rho^{\parallel}$ and $\rho^{\perp}$ to the asthenosphere of infinite extent differ by a factor of 1.5 to 2. In the case of the 300-km-wide asthenosphere, the difference reaches 5 to 10 times.

(4) The conductive connection of the continental asthenosphere with the oceanic asthenosphere is poorly reflected in both modes.

(5) The difference between continental conductors of infinite and finite lengths is better resolved in the TM mode as compared with the TE mode.

These conclusions agree with the results of trial inversions of synthetic data obtained in the coastal and central zones. The inversions were performed with the programs Inv2D-FG [Golubev and Varentsov, 1994] and IGF-MT2D [Novozhinskii and Pushkarev, 2001], which provide a regularized solution of the MT data inversion problem in the class of piecewise-uniform (block) media with a fixed geometry of boundaries. The inversion of the TE mode (longitudinal apparent resistivities, longitudinal impedance phases, and tipper

Table 2. MTS sensitivity to structures of the continental crust

Model element	Models compared	Zone	Sensitivity η	
			TE mode $\rho^{\parallel}$	TM mode $\rho^{\perp}$
Crustal conducting layer of infinite extent	I, II	ΔY_1	221%	214%
		ΔY_2	1285%	200%
		ΔY_3	1729%	950%
300-km-wide crustal conducting layer	I, III	ΔY_1	230%	25%
		ΔY_2	1333%	77%
		ΔY_3	1605%	109%
Downgoing conducting plate	I, III Crustal conducting layer of infinite extent	ΔY_1	442%	5%
		ΔY_2	34%	7%
		ΔY_3	2%	5%
	V, III 300-km-wide crustal conducting layer	ΔY_1	441%	4%
		ΔY_2	34%	7%
		ΔY_3	2%	5%
Junction of the downgoing slab with the crustal conducting layer	VI, IV Crustal conducting layer of infinite extent	ΔY_1	433%	2978%
		ΔY_2	104%	2646%
		ΔY_3	4%	674%
	VII, V 300-km-wide crustal conducting layer	ΔY_1	433%	1506%
		ΔY_2	103%	1184%
		ΔY_3	4%	192%

components) successfully reconstructs the crustal conducting layer and conducting continental asthenosphere. The inversion results of the TM mode (transverse apparent resistivities and transverse impedance phases) are appreciably worse (boundaries of the conducting layers are shifted and their resistivities substantially deviate from the true values). However, the TM mode more reliably determines the resistivity of the upper continental crust and fixes the junction of the slab with the crustal conducting layer.

An important result is that the model experiment demonstrated the possibility of determining the geoelectric structure of the crust and upper mantle from the frequency dependence of tipper components. This possibility is a natural consequence of the uniqueness theorem proven by V.I. Dmitriev for 2-D MV data inversion [Berdichevsky *et al.*, 1992].

5. 2-D OR 3-D INTERPRETATION?

To answer this question, we address 3-D regional near-surface heterogeneities crossed by the Lincoln line and elucidate how they influence the MT and MV sounding results.

Figure 9 plots the conductance *S* of the upper layer along the Lincoln line. The plot is based on bathymetric data and MT soundings from oceanic and continental segments of the profile. The conductance *S* in the deep ocean is on the order of 10000 S. The Coast Range, composed of Early Tertiary sediments and volcanic rocks, is characterized by a conductance of about 100 to 150 S. The volcanic–sedimentary complex of the western part of the Western Cascades and the thick sequence of Tertiary deposits filling the Willamette Valley are characterized by conductances reaching 250–300 S. In the eastern part of the Western Cascades, where these deposits wedge out, the conductance drops to 10 S. Beneath the High Cascades and the backarc plateau, the *S* values once again increase, reflecting the development of volcanic–sedimentary rocks underlying Late Tertiary and Quaternary volcanics.

Figure 10 presents a map showing the conductance *S* of the upper layer in a region encompassing the Juan de Fuca Ridge and plate with adjacent areas of the states of Oregon and Washington. In constructing this map, we used the map of sedimentary thickness [Connard *et al.*, 1984b] and estimated average resistivities of sediments. Oceanic features clearly recognizable in this map are the Juan de Fuca Ridge (I) and the abyssal basin of the Juan de Fuca plate (II). The following N–S-trending structures are traceable on the continent: the Coast Range (III), the Willamette Valley (IV) and the Puget Sound lowland extending the valley (V), the eastern Western Cascades (VI), and the High Cascades (VII). This detailed *S* map was incorporated into a less detailed map [Pal'shin *et al.*, 1999] covering the entire

Table 3. MTS sensitivity to structures of the continental mantle

Model element	Models compared	Zone	Sensitivity η	
			TE mode $\rho^{\parallel}$	TM mode $\rho^{\perp}$
Continental asthenosphere of infinite extent	VIII, VI Crustal conducting layer of infinite extent	ΔY_1	61%	48%
		ΔY_2	115%	55%
		ΔY_3	213%	88%
	XII, VII 300-km-wide crustal conducting layer	ΔY_1	72%	72%
		ΔY_2	141%	99%
		ΔY_3	309%	191%
300-km-wide continental asthenosphere	IX, VI Crustal conducting layer of infinite extent	ΔY_1	52%	10%
		ΔY_2	102%	8%
		ΔY_3	121%	9%
	XIV, VII 300-km-wide crustal conducting layer	ΔY_1	64%	28%
		ΔY_2	124%	23%
		ΔY_3	146%	34%
Junction between the continental and oceanic asthenosphere	X, VIII Crustal conducting layer of infinite extent 300-km-wide asthenosphere	ΔY_1	28%	18%
		ΔY_2	26%	18%
		ΔY_3	13%	17%
	X, VIII Crustal conducting layer of infinite extent 300-km-wide asthenosphere	ΔY_1	28%	14%
		ΔY_2	27%	13%
		ΔY_3	15%	12%
	XIII, XII 300-km-wide crustal conducting layer Asthenosphere of infinite extent	ΔY_1	28%	28%
		ΔY_2	27%	28%
		ΔY_3	13%	26%
	XV, XIV 300-km-wide crustal conducting layer 300-km-wide asthenosphere	ΔY_1	30%	23%
		ΔY_2	28%	22%
		ΔY_3	15%	20%

northwestern United States (1280 × 1280 km) and superimposed on a uniform background of S = 10 000 S. Estimates indicate that, in modeling the magnetotelluric field in the central part of this map, the influence of its edges may be neglected.

The 3-D MT field on the Lincoln line was calculated in the approximation of a nonuniform thin layer $S(x, y)$ underlain by a horizontally layered medium. As a section of this medium, we took the average continental section in the Cascadia subduction zone model from [Varentsov *et al.*, 1996]. The calculations were performed with the SLPROG program [Singer and Fainberg, 1985, 1995].

Figure 11 shows the continental 3-D curves of MT and MV soundings obtained at characteristic points of the Lincoln line. For comparison, this figure gives the corresponding locally normal 1-D and 2-D curves calculated for a 2-D model in which the $S(y)$ values specified on the Lincoln line were continued northward and southward (along the x direction). In the coastal and central zones (the Coast Range, Willamette Valley, and Western Cascades; y = 15–138 km), the curves $\rho^{\perp}_{3D}$, $\rho^{\parallel}_{3D}$, and $\mathrm{Re}\,W^{3D}_{zy}$ are similar to the curves $\rho^{\perp}_{2D}$, $\rho^{\parallel}_{2D}$, and $\mathrm{Re}\,W_{zy^{2D}}$ (the divergences are about 10% and, in any case, do not exceed 25%), and the curves $\varphi^{\perp}_{3D}$ and $\mathrm{Im}\,W^{3D}_{zy}$ virtually coincide with the curves $\varphi^{\perp}_{2D}$ and $\mathrm{Im}\,W^{2D}_{zy}$. In the far-field zone (the High Cascades and Deschutes Plateau; y = 158–178 km), the divergence between the curves $\rho^{\perp}_{3D}$ and $\rho^{\parallel}_{3D}$ reaches 100 to 200% (a strong static shift caused by 3-D volcanic–sedimentary structures), the curves $\mathrm{Re}\,W^{3D}_{zy}$ and $\mathrm{Im}\,W^{3D}_{zy}$ virtually coincide with the curves $\mathrm{Re}\,W^{2D}_{zy}$ and $\mathrm{Im}\,W^{2D}_{zy}$, and the curves $\varphi^{\perp}_{3D}$ and $\varphi^{\perp}_{2D}$ diverge only at high frequencies. It is noteworthy that the curves $\rho^{\parallel}_{3D}$ are similar to the locally normal (1-D) curves ρ_n nearly all along the Lincoln line. Evidently, the regional structure of near-surface rocks in the vicinity of the Lincoln line is favor-

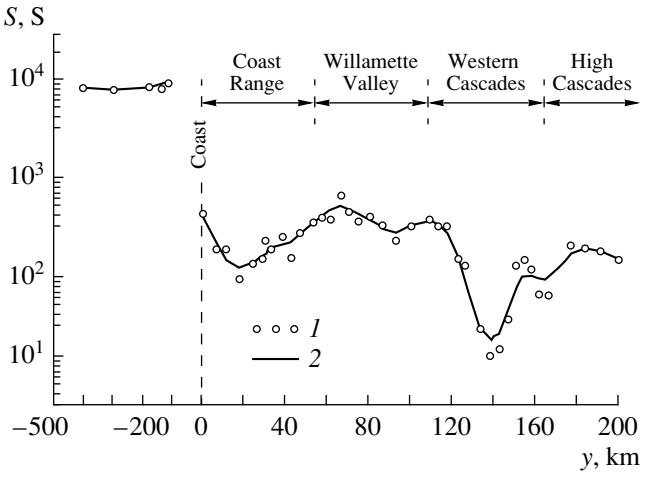

Fig. 9. Plot of the conductance *S* of the upper layer along the Lincoln line: (*1*) observations; (*2*) spline approximation.

able for a 2-D interpretation of MT and MV soundings. This important result fully agrees with the estimates obtained by Zhdanov and Spichak [1992] and Spichak [1999].

6. GEOELECTRIC MODELS EMSLAB-I AND EMSLAB-II

Two 2-D models of the Cascadia subduction zone are discussed most frequently in the geophysical literature: EMSLAB I [Wannamaker *et al.*, 1989b] and EMSLAB II [Varentsov *et al.*, 1996].

The EMSLAB I model is shown in Fig. 12. It was constructed by the trial-and-error method with a high priority given to the TM mode, which, according to the authors of the model, is most tolerant to deviations from two-dimensionality. This model minimizes the misfit between the $\rho^{\perp}$ and $\varphi^{\perp}$ curves and ignores the

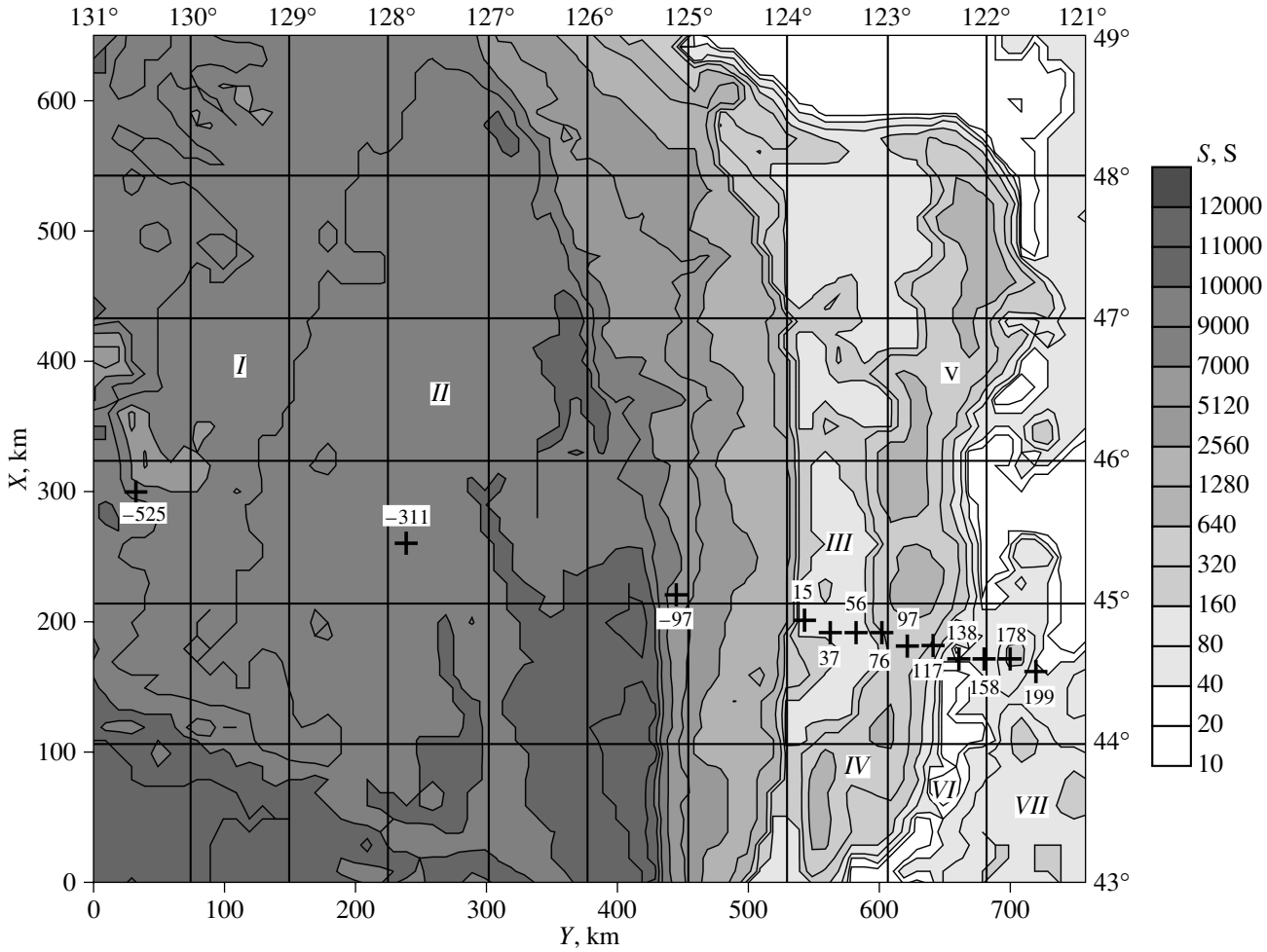

Fig. 10. Map showing the conductance *S* of the upper layer. Stations on the Lincoln line are indicated by crosses with distances from the coast (km).

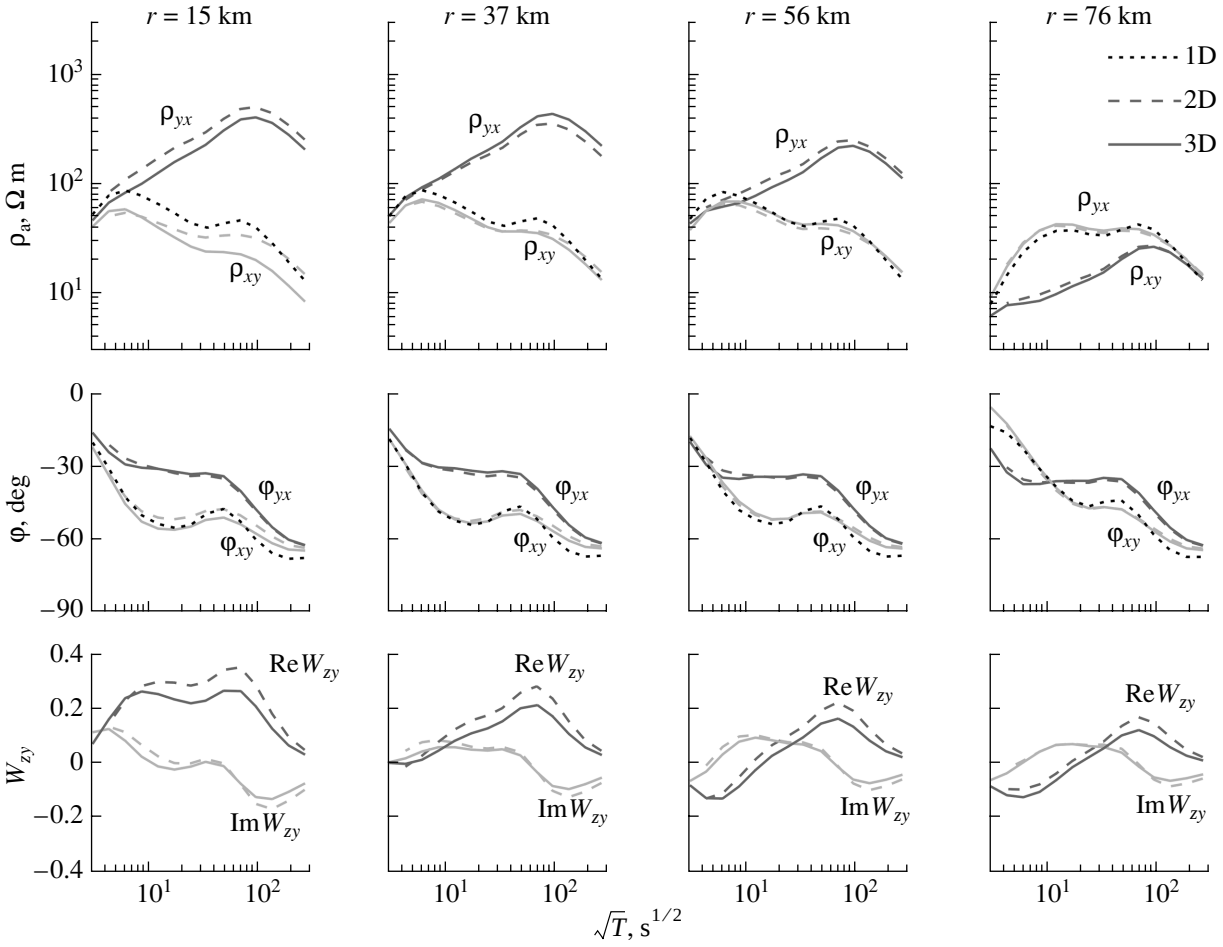

Fig. 11. 3-D curves ρ_{xy}, ρ_{yx}, φ_{xy}, φ_{yx}, $\mathrm{Re}\,W_{zy}$, and $\mathrm{Im}\,W_{zy}$ at points shown as crosses in Fig. 10 (continental segment of the Lincoln line). Also shown are the corresponding 2-D curves calculated for a 2-D model and locally normal 1-D curves calculated for a 1-D model.

$\rho^{\parallel}$ and $\varphi^{\parallel}$ curves. The main elements in the EMSLAB I model are (1) the upper conducting part of the plate subducting under the Coast Range at a low angle; (2) a subhorizontal conducting layer in the middle continental crust thickening under the High Cascades; and (3) a well-developed conducting asthenosphere under the ocean. The question of whether the downgoing slab is connected with the crustal conductor is left open in the EMSLAB I model. No continental asthenosphere is present in this model, although the shape of the experimental $\rho^{\parallel}$ and $\varphi^{\parallel}$ curves indicates a low resistivity of the upper mantle. The absence of gross discrepancies between the model $\mathrm{Re}\,W_{zy}$ and $\mathrm{Im}\,W_{zy}$ values and observational data is regarded by the authors of the model as evidence of its reliability.

The EMSLAB I model is vulnerable to criticism. A cold continental mantle contradicts the modern geodynamic concepts of the Cascadia subduction zone (compare EMSLAB I with the predictive model CASCADIA shown in Fig. 5). Subsequent analysis of the EMSLAB I model showed that the TM mode has a low sensitivity to variations in the mantle conductivity and that only bimodal inversion using both modes (TE + TM) can provide a key to studying the asthenosphere (see [Berdichevsky *et al.*, 1992], where Dmitriev's bimodal algorithm based on successive inversion of the TE and TM modes is described). This algorithm ensures better conditions for an interactive target interpretation of MT data taking into account the different informativeness of the TE and TM modes.

Experiments on the bimodal interpretation of MT data from the Cascadia subduction zone resulted in the development of the 2-D EMSLAB II model (Fig. 13). It was constructed with the INV2D-FG program designed for automated inversion and enabling optimization of resistivities in 20 blocks with a fixed geometry. The program is based on Dmitriev's algorithm, consisting of three successive levels: (1) inversion of $\varphi^{\perp}$ and $\mathrm{Re}\,W_{zy}$ (maximum weight); (2) inversion of $\varphi^{\parallel}$ and $\rho^{\perp}$ (normal weight); and (3) inversion of $\rho^{\parallel}$ (minimum

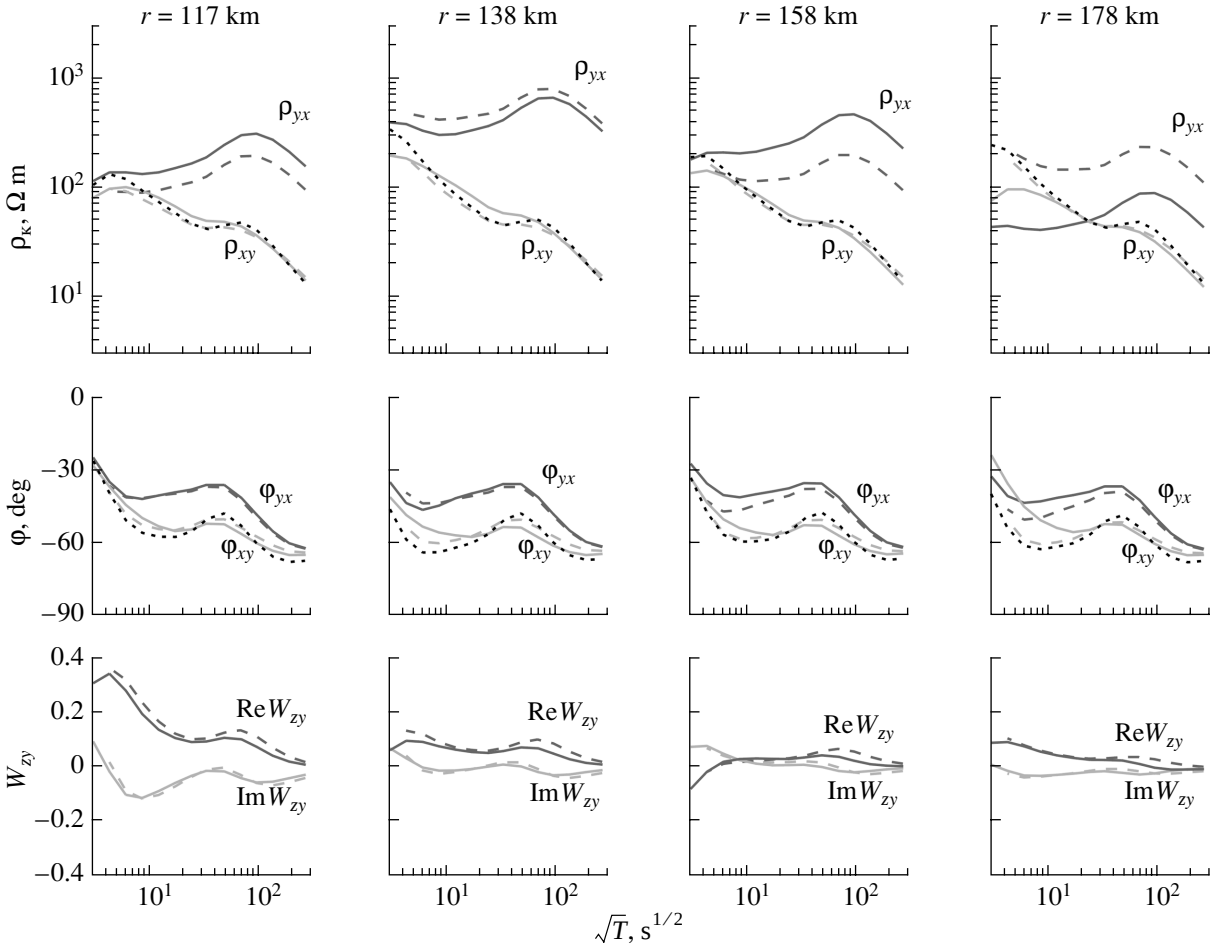

Fig. 11. (Contd.)

weight). The EMSLAB II model has much in common with the EMSLAB I: the same oceanic asthenosphere, the same downgoing plate, and the same crustal conducting layer. However, the plate is connected with the crustal conductor, and the continental mantle contains a conducting asthenosphere (!) separated from the oceanic asthenosphere. Thus, new evidence for partial melting in the continental mantle was obtained. The main drawback of the EMSLAB II model is its schematism due to the limitations of the INV2D-FG program.

At present, INV2D-FG has been superseded by more effective programs for 2-D automated inversion of MT and MV data. They include the smoothing program REBOCC, implementing Occam's razor[1] [Siripunvaraporn and Egbert, 2000], and the programs IGF-MT2D [Novozhinskii and Pushkarev, 2001] and II2DC [Varentsov, 1999], which enable the optimization of models containing 512 and more blocks of a fixed geometry. Thus, new possibilities have opened for the interpretation of EMSLAB data, and we use them for constructing the model EMSLAB III.

7. ANALYSIS OF OBSERVATIONS ON THE LINCOLN LINE

Observations on the continental segment of the Lincoln line yielded the frequency characteristics of the MT tensor (impedance) [**Z**] and the MV tensor (tipper) [**W**]:

$$[\mathbf{Z}] = \begin{bmatrix} Z_{xx} & Z_{xy} \\ Z_{yx} & Z_{yy} \end{bmatrix} \quad [\mathbf{W}] = \begin{bmatrix} W_{zx} & W_{zy} \end{bmatrix}.$$

These tensors transform the horizontal magnetic field $\mathbf{H}_\tau$ into the horizontal electric field $\mathbf{E}_\tau$ and the vertical magnetic field H_z, respectively:

$$\mathbf{E}_\tau = [\mathbf{Z}]\mathbf{H}_\tau \quad H_z = [\mathbf{W}]\mathbf{H}_\tau.$$

By analyzing [**Z**] and [**W**], it is possible to assess the degree of horizontal inhomogeneity of the medium, recognize the field distortions due to the heterogeneity of the medium, identify geoelectric structures, and

[1] The razor principle was formulated by the Franciscan monk William of Occam in the 14th century. In modern terms, it might be phrased as follows: "Do not multiply complex assumptions where a simple explanation would be sufficient."

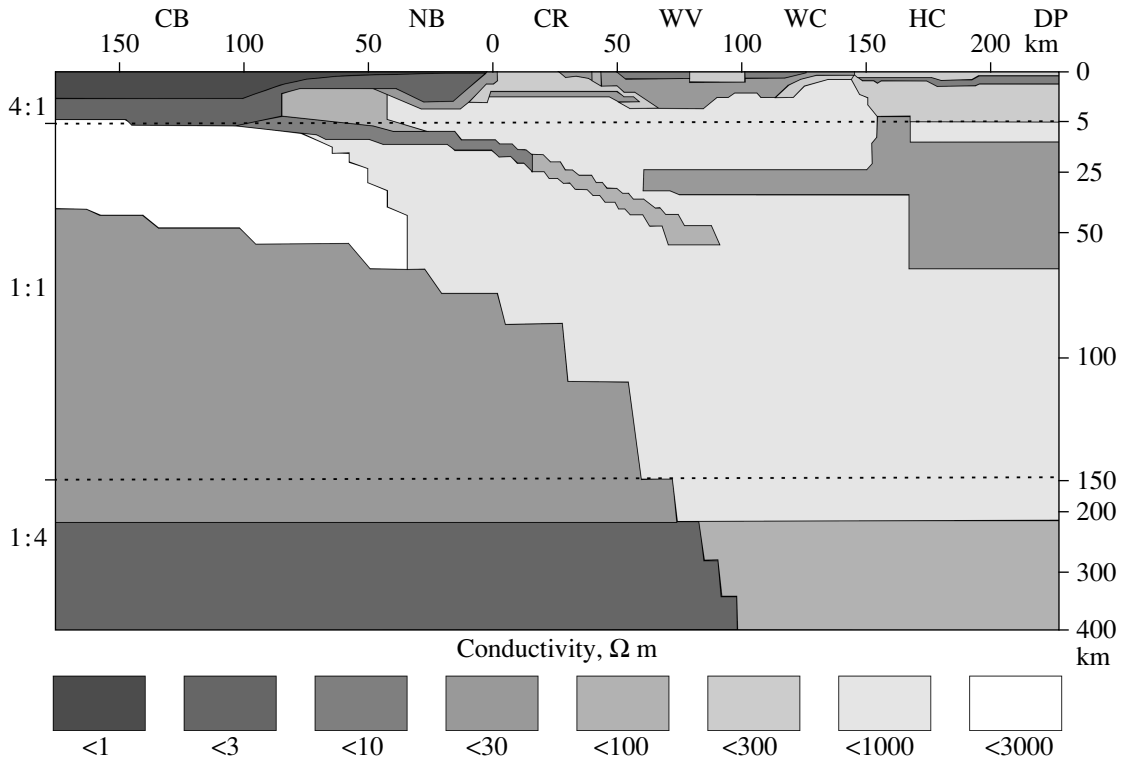

Fig. 12. The EMSLAB I model [Wannamaker *et al.*, 1989b]: CB, Cascadia Basin; NB, Newport Basin; CR, Coast Range; WV, Willamette Valley; WC, Western Cascades; HC, High Cascades; DP, Deschutes Plateau.

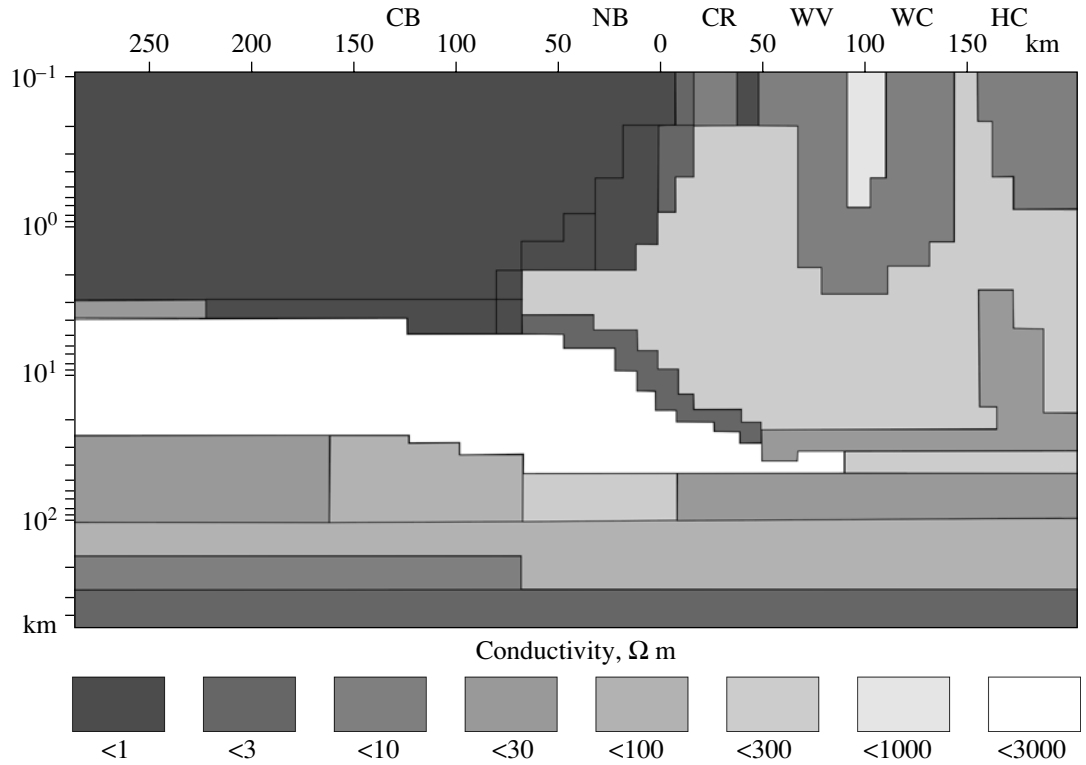

Fig. 13. The EMSLAB II model [Varentsov *et al.*, 1996]. Notation is the same as in Fig. 12.

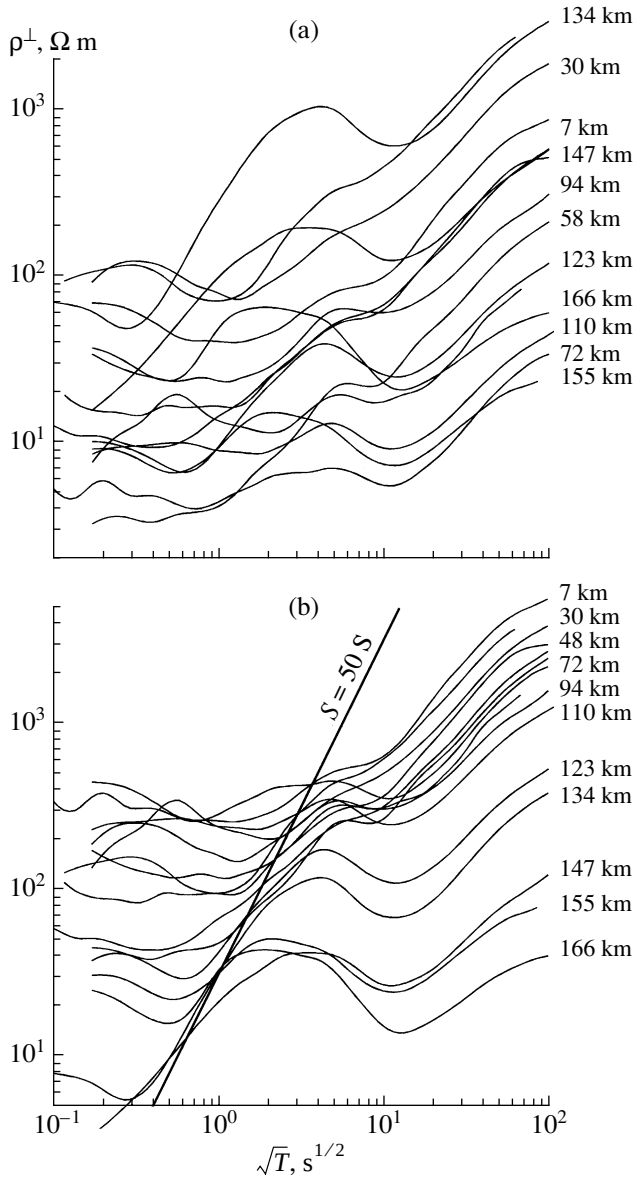

Fig. 14. Transverse apparent resistivity ($\rho^{\perp}$) curves along the continental part of the Lincoln line: (a) observed and (b) normalized curves. The parameter of the curves is the distance to the shoreline.

determine their dimensions and trends. Thus, we obtain a basis for constructing an interpretation model (determination of the class of media in which the solution to the inverse problem is sought).

Figure 14a shows transverse apparent resistivity curves in a period range of 0.01–10000 s. The curves consist of two ascending branches separated by an inflection or a minimum. The right-hand ascending branches of these curves have identical slopes and account for nearly two decades. For a better understanding of the phenomena observed, we normalize the $\rho^{\perp}$ curves by vertically shifting them in order that their left ascending branches fit best the line of the average conductance $\bar{S}$ = 50 S of the upper layer (Fig. 14b). These normalized $\rho^{\perp}$ curves demonstrate a simple regular pattern: the greater the distance from the coast, the deeper the central minimum of these curves and the lower their right-hand branches. Comparing this figure with Fig. 6, we find an unquestionable similarity between the behavior of the normalized $\rho^{\perp}$ curves obtained on the Lincoln line and the theoretical $\rho^{\perp}$ curves calculated for the models A and S. It seems evident that the continental trap effect is observable on the Lincoln line and that precisely this effect rather than the influence of lithospheric and asthenospheric structures controls the transverse $\rho^{\perp}$ curves obtained at various distances from the coast.

The longitudinal apparent resistivity curves obtained in the same period range are shown in Fig. 15. With increasing distance from the coast, the $\rho^{\parallel}$ curves change in shape, occasionally showing bell- and cup-shaped branches. Distinctive features of the $\rho^{\parallel}$ curves are low-frequency, gently descending branches lying on various levels. At points 2, 3, 4, and 12, these descending branches terminate in a more or less steep ascent. One might assume that the longitudinal $\rho^{\parallel}$ curves reflect variations in the geoelectric structure of the lithosphere and asthenosphere but are distorted by a static shift and 3-D channeling effects.

Note that the $\rho^{\perp}$ curves are connected with the $\varphi^{\perp}$ curves via dispersion relations at all points of the Lincoln line [Berdichevsky and Pokhotelov, 1997]. However, the $\rho^{\parallel}$ and $\varphi^{\parallel}$ curves (in contrast to the $\rho^{\perp}$ and $\varphi^{\perp}$ curves) episodically violate the dispersion relations (point 3, 4, 10, and 13), as is seen in Fig. 16.

Now we address the analysis of MT parameters: the inhomogeneity parameter N [Berdichevsky *et al.*, 1997], the skew parameter [Swift, 1967], and the phase-sensitive skew parameter η [Bahr, 1988]. The N, skew, and η values are determined by the formulas

$$N = \left| \sqrt{1 - 4\frac{Z_{xx}Z_{yy} - Z_{xy}Z_{yx}}{(Z_{xy} - Z_{yx})^2}} \right|,$$

$$\text{skew} = \left| \frac{Z_{xx} + Z_{yy}}{Z_{xy} - Z_{yx}} \right|, \quad \eta = \frac{\sqrt{0.5\left|\text{Im}(Z_{xy}Z_{yy}^* + Z_{xx}Z_{yx}^*)\right|}}{\left|Z_{xy} - Z_{yx}\right|},$$

where the asterisk (*) indicates complex conjugation. In a 1-D (horizontally uniform) model, N = skew = η = 0. The deviation of N from 0 is a measure of the horizontal nonuniformity of the medium. In a 2-D model, $N \neq 0$ and skew = η = 0. In a 3-D model, $N \neq 0$, skew $\neq 0$, and $\eta \neq 0$. If the model has a 2-D structure complicated by small near-surface 3-D inclusions, $\eta = 0$ at low frequencies, whereas $N \neq 0$ and skew $\neq 0$. Thus, combined analysis of the parameters N, skew, and η makes it possible to identify structures and determine their dimensionality.

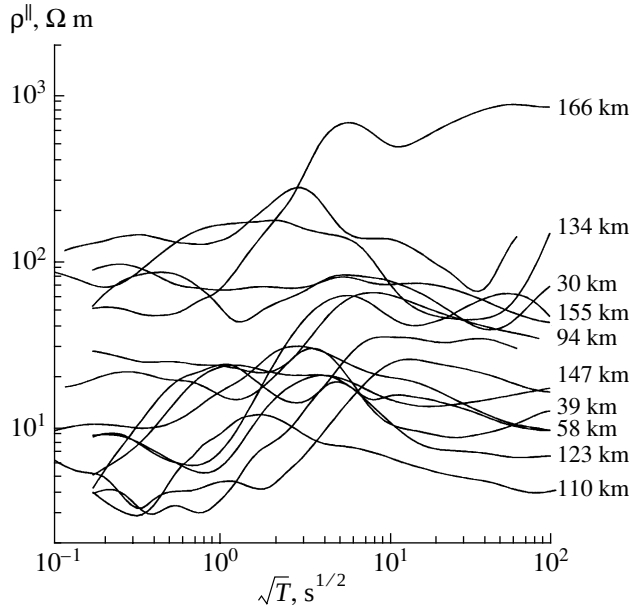

Fig. 15. Longitudinal apparent resistivity ($\rho^{\parallel}$) curves along the continental part of the Lincoln line. The parameter of the curves is the distance to the shoreline.

Figure 17 presents frequency sections of N, skew, and η. At high frequencies ($T \ll 1$ s), the nonuniformity parameter N is nearly everywhere no more than 0.1–0.2, indicating the validity of 1-D resistivity estimates for near-surface rocks. At $T = 1$ s, N varies from 0.1–0.2 in the Willamette Valley and High Cascades to 0.4 in the Coast Range and Western Cascades. With decreasing frequency ($T > 100$ s), N increases to 0.4 in the Willamette Valley and to 0.5–0.8 in the Coast and Cascade ranges. High N values are usually associated with elevated values of skew (0.3–0.7) and small values of η (<0.1–0.15). Thus, following Bahr [1988], we can regard the medium under study as a regionally 2-D structure with local 3-D heterogeneities in its upper horizons. Deep 3-D effects are possible only beneath the High Cascades, where low-frequency η values exceed 0.3. The azimuth of the regional trend of deep 2-D heterogeneities determined from the Bahr expansion varies from 7.5° to 10°. This agrees with the orientation of low-frequency polar plots of the magnetic tensor and induction arrows at many points on the Lincoln line. For illustration, Fig. 18 shows magnetic polar diagrams for $T = 2500$ and real parts of induction arrows for $T = 6400$ s. Within the Coast Range, the magnetic diagrams are figures of eight with their major axis oriented roughly E–W. Similar diagrams are typical of the Willamette Valley and the High Cascades. Within the High Cascades, magnetic diagrams degenerate into ovals but retain an E–W orientation. The real induction arrows are everywhere directed from west to east.

It is clear that, in the EMSLAB experiment, we can seek a solution to the inverse geoelectrical problem in the class of N–S-trending 2-D media.

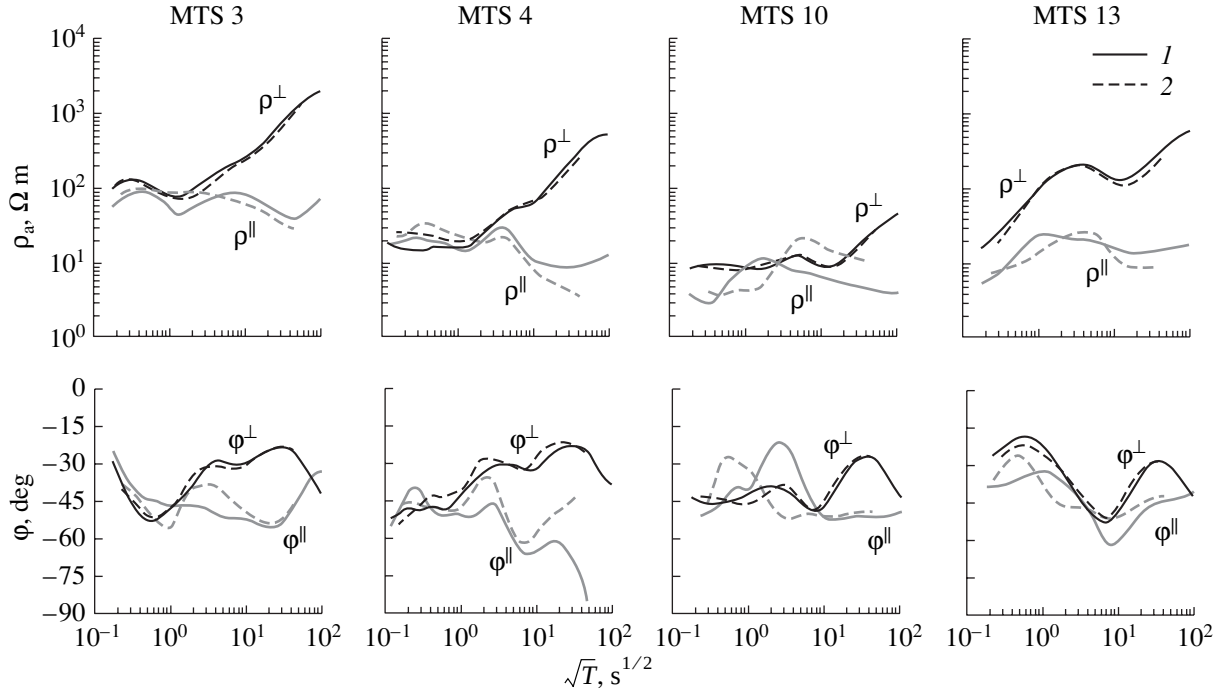

Fig. 16. Dispersion relations between apparent resistivity (ρ_a) and phase (φ) curves: (*1*) observations; (*2*) dispersion transformation.

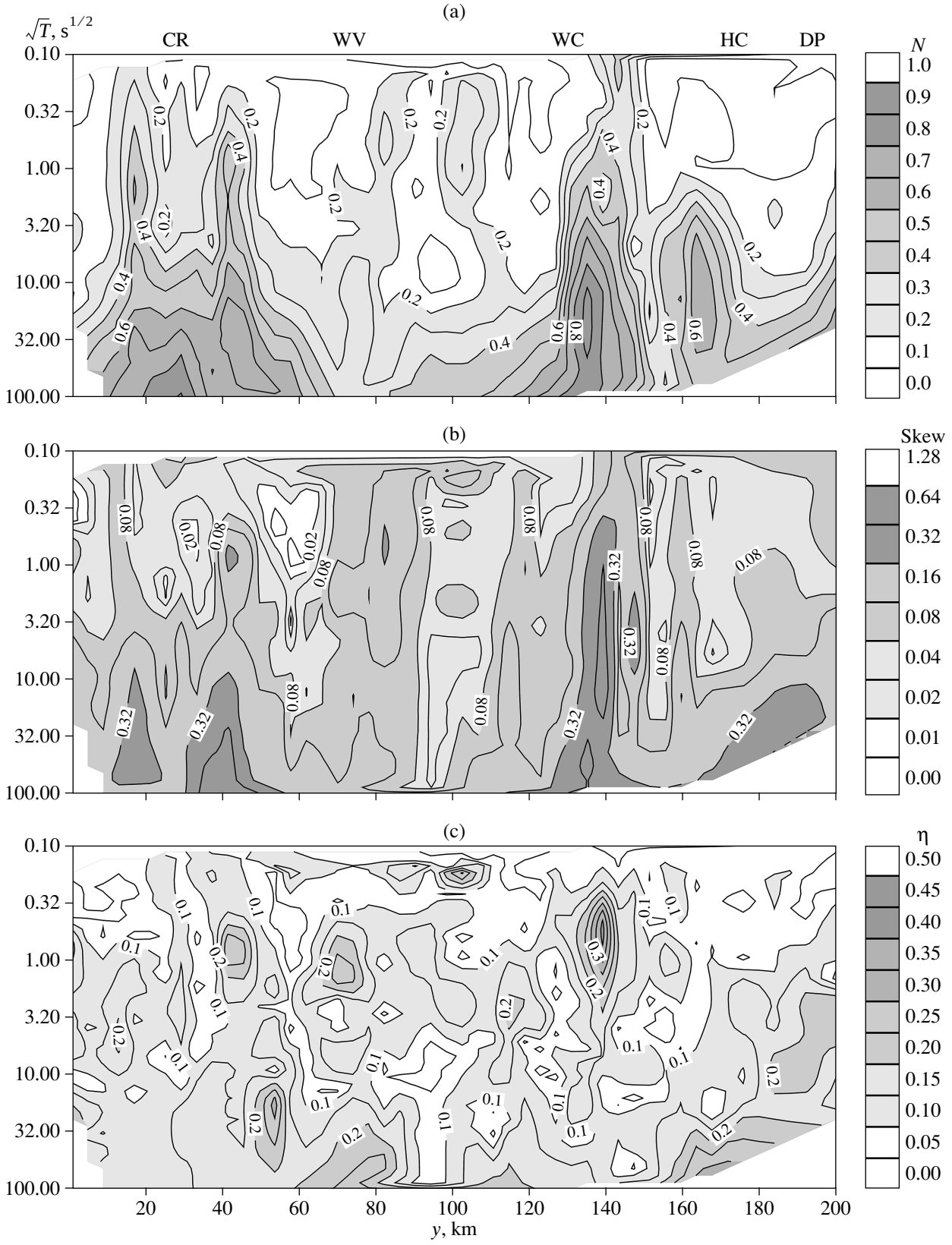

Fig. 17. Frequency sections of the parameters of (a) inhomgeneity *N*, (b) skew, and (c) phase-sensitive skew η: CR, Coast Range; WV, Willamette Valley; WC, Western Cascades; HC, High Cascades; DP, Deschutes Plateau.

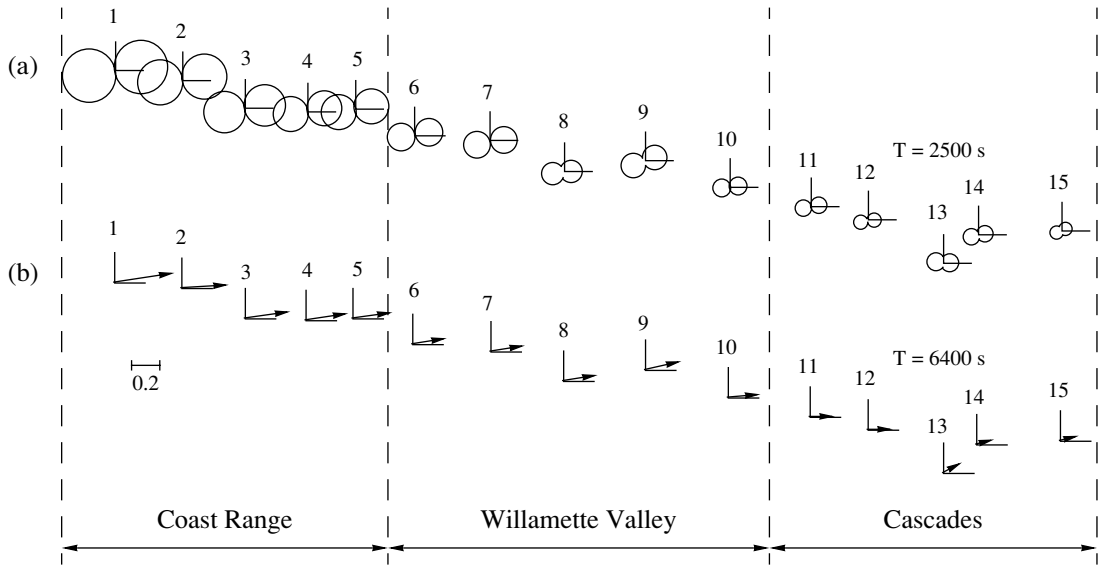

Fig. 18. Magnetic polar diagrams and real induction arrows along the continental part of the Lincoln line: (a) polar diagrams of the tipper at the period T = 2500 s; (b) real induction arrows at the period T = 6400 s.

8. A NEW GEOELECTRICAL MODEL OF CASCADIA: EMSLAB III

The 2-D inversion of MT and MV data is a multicomponent inverse problem using (1) real and imaginary tippers ($\mathrm{Re}\,W_{zy}$ and $\mathrm{Im}\,W_{zy}$, 2); (2) longitudinal and transverse apparent resistivities ($\rho^{\parallel}$ and $\rho^{\perp}$); and (3) longitudinal and transverse impedance phases ($\varphi^{\parallel}$ and $\varphi^{\perp}$). These components differ in informativeness, sensitivity to the distorting influence of near-surface heterogeneities, and sensitivity to the structures under study.

We distinguish $\mathrm{Re}\,W_{zy}$ and $\mathrm{Im}\,W_{zy}$ as components that are, first, sensitive to conducting structures and, second, become insensitive to near-surface effects with decreasing frequency. Moreover, Dmitriev recently proved the uniqueness theorem for the 2-D inversion of tipper components [Berdichevsky *et al.*, 2000]. It is clear that the interpretation of the frequency characteristics of $\mathrm{Re}\,W_{zy}$ and $\mathrm{Im}\,W_{zy}$ can give reliable constraints on conducting zones in the crust and mantle.

The longitudinal apparent resistivities $\rho^{\parallel}$ and phases $\varphi^{\parallel}$ are also sensitive to conducting structures. However, if the $\rho^{\parallel}$ curves are subjected to the distorting effect of near-surface heterogeneities, their interpretation involves the problem of static shifts. The correction of static shifts in $\rho^{\parallel}$ curves can lead to serious errors. This makes the longitudinal apparent resistivity $\rho^{\parallel}$ less reliable than tipper components. The longitudinal phase $\varphi^{\parallel}$ is somewhat more effective because, similar to the tipper, it becomes insensitive to near-surface effects with decreasing frequency. However, even the analysis of 1-D MTS curves indicates that phase inversion yields a conductivity distribution accurate to unknown scale factors. Evidently, the phases $\varphi^{\parallel}$ are less informative than the apparent resistivities $\rho^{\parallel}$, and the interpretation of the $\varphi^{\parallel}$ curves is meaningful only in conjunction with the interpretation of the curves $\rho^{\parallel}$ or $\mathrm{Re}\,W_{zy}$ and $\mathrm{Im}\,W_{zy}$.

The transverse apparent resistivities $\rho^{\perp}$ and phases $\varphi^{\perp}$ are characterized by a reduced (if not vanishing) sensitivity to conducting structures overlain by a low-conductivity medium (the galvanic screening effect). However, they allow one to estimate the resistivity of low-conductivity lithospheric layers and, in a favorable case, to reveal relationships between conducting structures (e.g., to discover faults reaching the sedimentary cover or the junction between the subducting conductive plate and crustal conductive layer). An evident problem in interpreting the $\rho^{\perp}$ curves is the static shift, but this effect can be eliminated through an automatic correction applied during the inversion.

There exist two approaches to the solution of the multicomponent inversion problem:

(I) Parallel (joint) inversion of all components, which are introduced into the Tikhonov functional with different weights depending on their informativeness, stability, and sensitivity.

(II) Successive (partial) inversions of each component, with the transfer of the weighted inversion results from one component to another.

The following considerations favor the second approach. Partial inversions are most convenient for interactive interpretation of geoelectric data. Each partial inversion solves a certain particular problem and can be focused on a specific structure by means of spatial and frequency-related weightings. The results of each partial inversion can be transferred to a subsequent

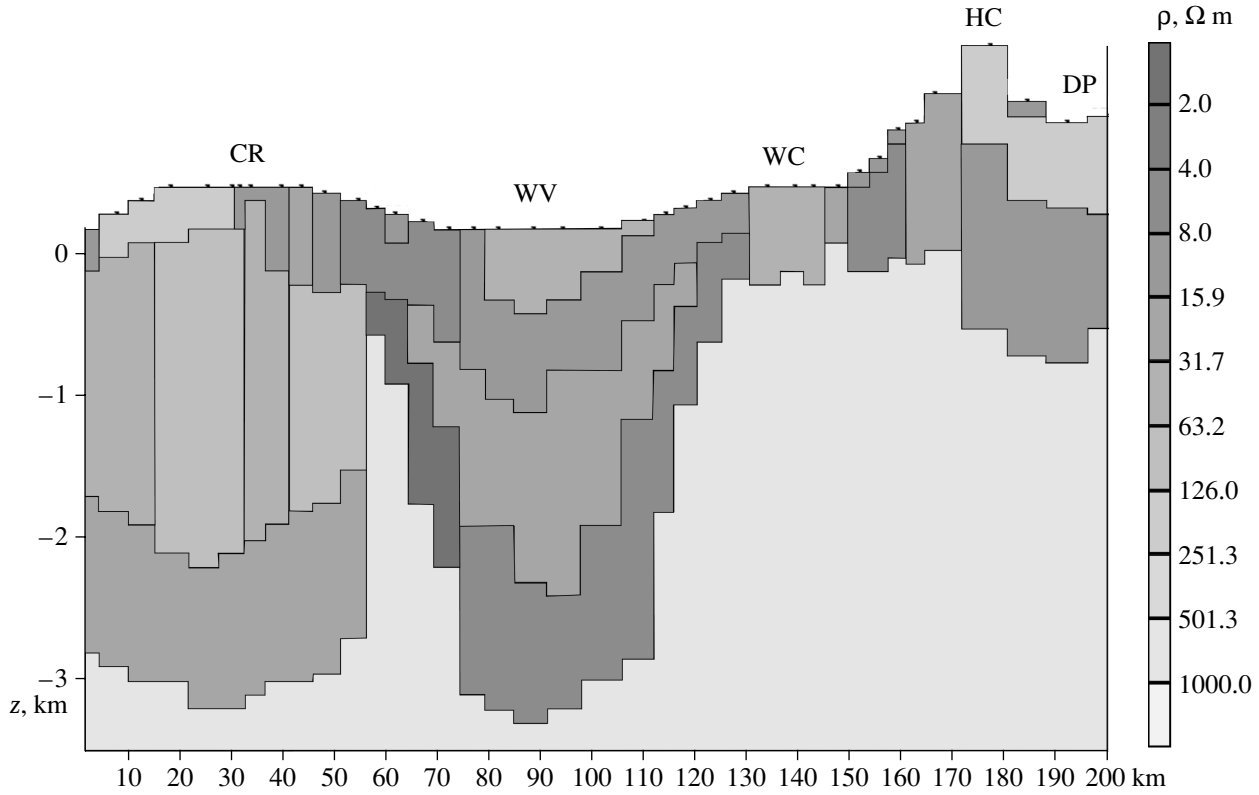

Fig. 19. Geoelectric structure of the volcanic–sedimentary cover (continental part of the Lincoln line). Notation is the same as in Fig. 17.

inversion with weights that are determined by information analysis and reflect the degree of confidence in particular structures. Partial inversions admit the updating of results directly during the interpretation process. Partial inversions decrease the probability that the misfit will fall into a local minimum. The entire experience of Russian deep geoelectrics indicates that this approach, based on a sequence of partial inversions and easily implementable by means of the Dmitriev's multilevel algorithm, ensures the most comprehensive interpretation of electromagnetic soundings.

We applied the method of partial inversions to the interpretation of data obtained on the Lincoln line. The interpretation consisted of three stages.

At the first stage, we performed 1-D inversion of short-period MT curves (T = 0.01–100 s) and constructed an approximate geoelectric section of the volcanic–sedimentary cover to a depth of 3.5 km (Fig. 19). This section, consistent with the near-surface part of the EMSLAB I model [Wannamaker *et al.*, 1989b], was incorporated into the starting 2-D interpretation model.

At the second stage, we used the REBOCC program incorporating the Occam principle and conducted experiments with a smoothed 2-D inversion. Under the complex conditions of the Cascadia subduction zone, the joint inversion of the TE and TM modes yields intricately alternating low- and high-resistivity spots with a poor misfit minimization. Such a pattern yields very poor constraints on real structures of the subduction zone. The most interesting result was obtained from the partial inversion of the TE mode (Fig. 20): the western and eastern conducting zones were found to be separated by a T-shaped high-resistivity structure that can be associated with the downgoing plate. An oceanic asthenosphere with its top fixed at a depth of about 20 km is recognizable in the western conducting zone. The eastern conducting zone is confined to the crust–mantle region of wet melting derived from the predictive CASCADIA model shown in Fig. 5. It is noteworthy that the upper boundary of the eastern conducting zone resembles the relief of the crustal conducting layer from the models EMSLAB I and EMSLAB II (see Figs. 12 and 13).

At the third, final, stage we applied the method of partial inversions and constructed a new geoelectric model of the Cascadia subduction zone called the EMSLAB III model. Long-period MV and MT curves (T = 1–10000 s) were interpreted with the programs IGF-MT2D [Novozhinskii and Pushkarev, 2001] and II2DC [Varentsov, 1999], implementing the misfit minimization in the class of media with a fixed geometry of blocks. The interpretation was conducted in a hypothesis-testing mode. Three hypotheses of the Cascadia

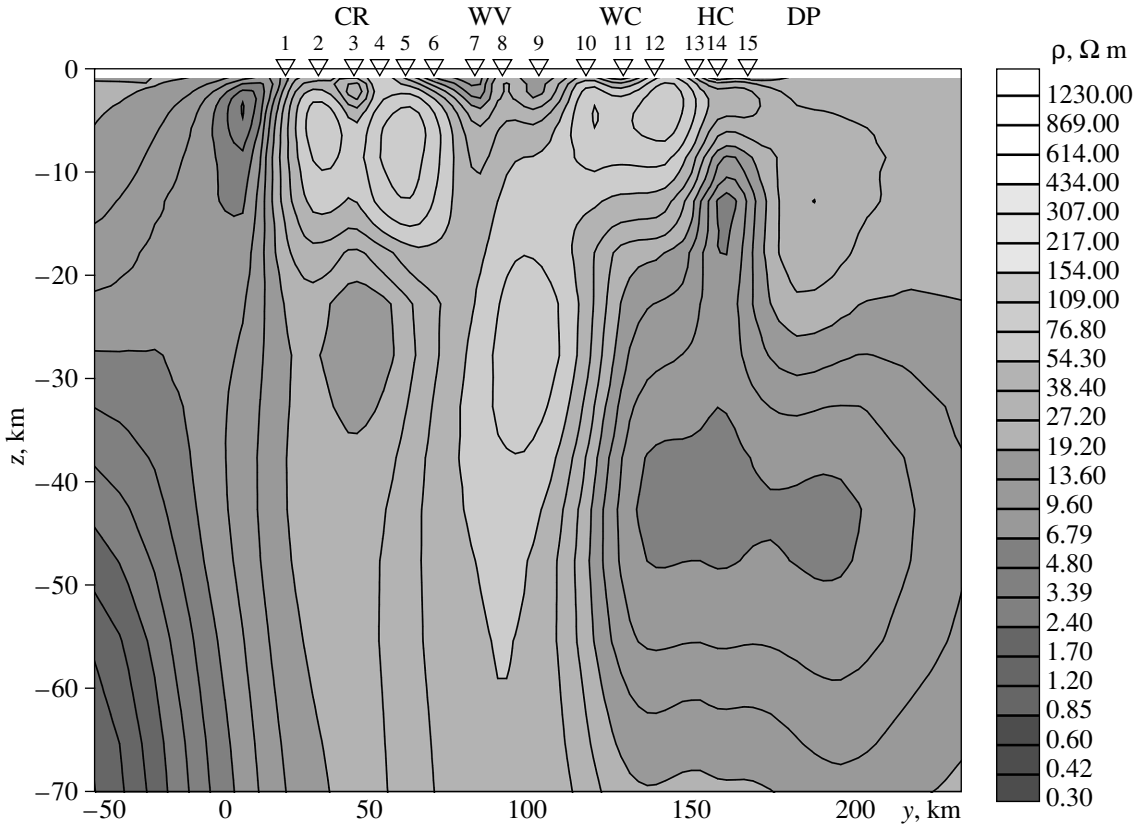

Fig. 20. 2-D REBOCC inversion of the TE mode (Re W_{zy}, Im W_{zy}, and $\varphi^{\parallel}$). Notation is the same as in Fig. 17.

structure were examined; these are hypotheses underlying (1) the EMSLAB I model (Fig. 12), (2) EMSLAB II model (Fig. 13), and (3) predictive CASCADIA model (Fig. 5).

The starting interpretation model (START model) is shown in Fig. 21. The seafloor topography and thicknesses of bottom sediments, as well as sediments of the accretionary prism and shelf, were specified from the bathymetric and sedimentary thickness maps [Conrad *et al.*, 1984a, 1984b]. The resistivities of water, sediments, and oceanic crust were set at 0.3, 2, and 10000 Ω m, respectively. The depth to the oceanic mantle and its resistivities were taken in conformity with the models CASCADIA, EMSLAB I, and EMSLAB II. The surface of the subducting oceanic plate was reconstructed from seismic data [Trehu *et al.*, 1994] and seismic tomography imagery [Weaver and Michaelson, 1985; Rasmussen and Humphries, 1988]. The structure of the continental volcanic–sedimentary cover was determined from the results of 1-D inversion of short-period MT curves. The continental crust and mantle were divided into uniform blocks having a resistivity of 1000 Ω m. The distribution density and geometry of the blocks allow a free choice of crustal and mantle structures consistent with the three hypotheses examined. The hypothesis that best fits observations was selected automatically in the process of resistivity optimization and misfit minimization. The uncertainty intervals for the resistivities being optimized were specified depending on the reliability of the starting constraints. Minimum intervals were assigned to blocks composing the continental volcanic–sedimentary cover and ocean floor (bottom sediments and oceanic crust), and maximum intervals were assigned to blocks accounting for the continental lower crust and mantle.

The MTS method plays a leading role in the traditional scheme of deep electromagnetic sounding, while MV data are used to check and refine the MTS results. This scheme is widely and often successfully applied. Its weakness lies in the fact that the low-frequency MT impedance is subjected to the distorting effect of near-surface heterogeneities. In this work, we use a scheme of deep electromagnetic sounding in which the leading method is MV sounding, whereas MTS serves to check and refine the MV results. The main advantage of this scheme is that the MV tipper is insensitive to the distorting effect of near-surface heterogeneities at lower frequencies. It is clear that, in this way, we substantially improve the reliability of geoelectric information.

MV and MT data obtained at 15 stations on the Lincoln line (T = 1–10000 s) were successively interpreted on four levels. The interpretation algorithm is presented

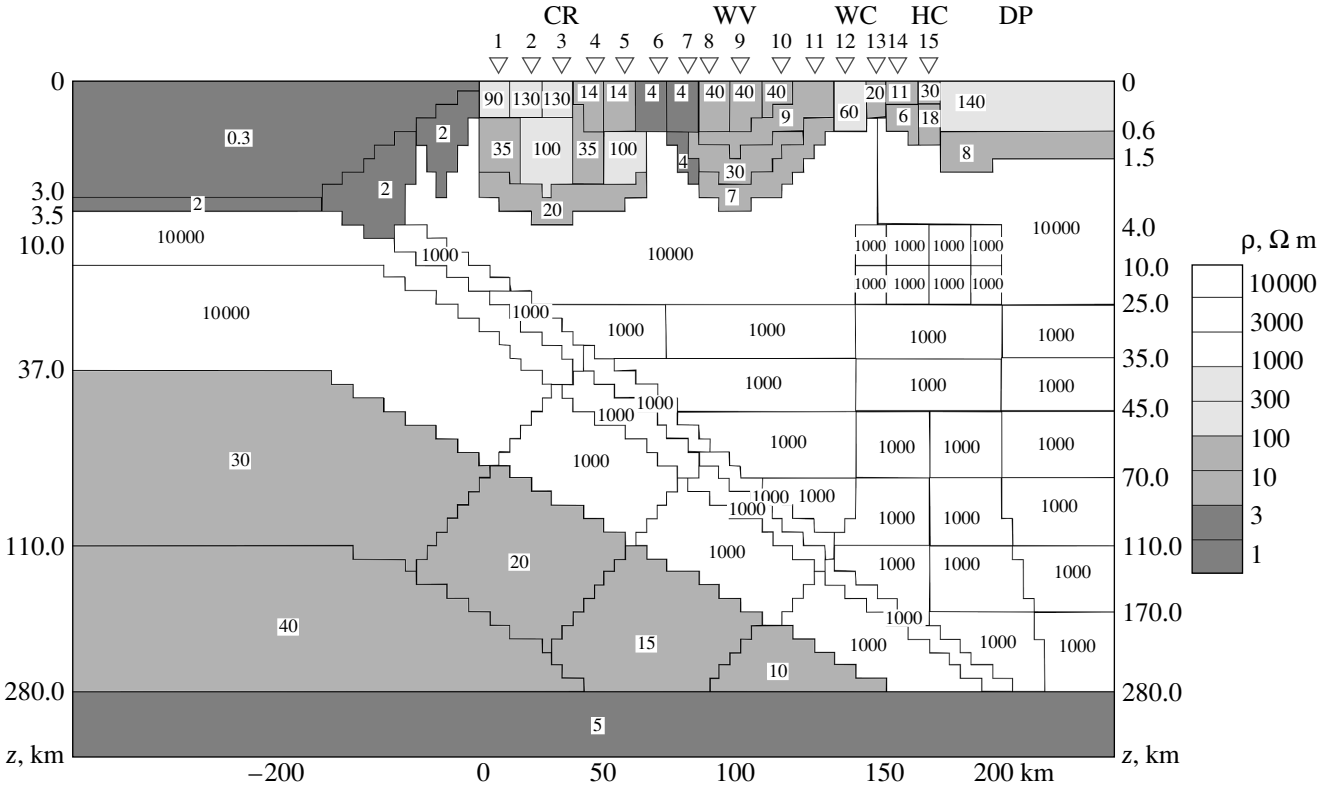

Fig. 21. Starting START interpretation model: CR, Coast Range; WV, Willamette Valley; WC, Western Cascades; HC, High Cascades; DP, Deschutes Plateau. Numbers within blocks are resistivities (Ω m).

in Fig. 22. The inversions performed on each level are described below.

Level I: inversion of $\mathrm{Re}\,W_{zy}$ and $\mathrm{Im}\,W_{zy}$. The START model was taken as the starting model. The inversion yielded the TP model shown in Fig. 23. The model residuals are given in Table 4. Here, $\delta(\mathrm{Re}\,W_{zy})$ and $\delta(\mathrm{Im}\,W_{zy})$ are the residuals of the real and imaginary tippers (rms deviations of the model results from the observed values); $\Delta\mathrm{Re}\,W_{zy} = |\max\mathrm{Re}\,W_{zy} - \min\mathrm{Re}\,W_{zy}|$ and $\Delta\mathrm{Im}\,W_{zy} = |\max\mathrm{Im}\,W_{zy} - \min\mathrm{Im}\,W_{zy}|$ characterize the maximum variation in the observed values of the real and imaginary tippers. The TP model is seen to agree well with observations: at most stations, the residuals $\delta\mathrm{Re}\,W_{zy}$ and $\delta\mathrm{Im}\,W_{zy}$ are at least 5 to 10 times lower than the maximum tipper variations. A noteworthy feature of this model is a conducting continental asthenosphere with a branching-out vertical low-resistivity zone penetrating the continental crust under the High Cascades. This feature of the TP model distinguishes it from EMSLAB I and EMSLAB II and makes it similar to the predictive CASCADIA model, in which a vertical high-temperature zone of wet and dry melting evidently characterized by low resistivities is localized beneath the High Cascades. The test of a TP model without the continental asthenosphere and vertical crustal high-resistivity zone increased the model residual by factors of 1.5 to 2.5. Thus, we conclude that the tipper inversion settles the dispute among the three hypotheses in favor of the CASCADIA model.

Level II: inversion of $\varphi^{\parallel}$. On this level, we check the results of tipper inversion in terms of the TE mode. The inversion of the $\rho^{\parallel}$ curves distorted by near-surface heterogeneities requires a preliminary normalization of the

Table 4. Residuals of $\mathrm{Re}W_{zy}$ and $\mathrm{Im}W_{zy}$

Point	1	2	3	4	5	6	7	8	9	10	11	12	13	14	15
$\delta\mathrm{Re}W_{zy}$	0.07	0.04	0.03	0.06	0.03	0.02	0.02	0.02	0.03	0.05	0.02	0.04	0.04	0.05	0.02
$\delta\mathrm{Im}W_{zy}$	0.05	0.05	0.03	0.04	0.01	0.02	0.02	0.02	0.02	0.03	0.02	0.02	0.05	0.04	0.03
$\Delta\mathrm{Re}W_{zy}$	0.39	0.37	0.3	0.47	0.59	0.51	0.24	0.25	0.27	0.23	0.41	0.48	0.42	0.42	0.36
$\Delta\mathrm{Im}W_{zy}$	0.37	0.26	0.27	0.23	0.31	0.29	0.1	0.11	0.16	0.17	0.26	0.18	0.26	0.17	0.12

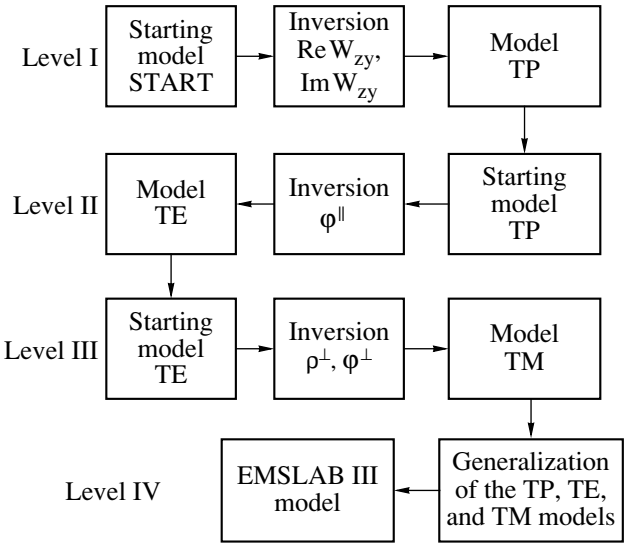

Fig. 22. Sequence of partial inversions.

apparent resistivities, which almost always involves the risk of errors (especially in mountains). Therefore, interpreting the EMSLAB data, we limited ourselves to the inversion of $\varphi^{\parallel}$ curves whose low-frequency branches are weakly distorted at most stations. If the $\rho^{\parallel}$ and $\varphi^{\parallel}$ curves are connected via dispersion relations, we hardly lose any substantial information while applying this approach. The normalization of the $\varphi^{\parallel}$ curves reduces to a rejection of regions in which the dispersion relations are strongly violated and an elimination of short low-frequency ascending branches that appear to be due to local effects of 3-D channeling. The starting model was the TP model derived from the tipper inversion. The inversion of the longitudinal phases yielded the TE model shown in Fig. 24. The phase inversion residuals are presented in Table 5, where, $\delta\varphi^{\parallel}$ is the phase residual (rms deviation of the model values from the observed values), and $\Delta\varphi^{\parallel} = |\max\varphi^{\parallel} - \min\varphi^{\parallel}|$ characterizes the maximum variation of the observed phase values.

At most stations, the phase residuals are 5 to 10 times lower than the phase maximum variation, indicating good agreement between the model and observations. Now we compare the TE and TP models. The TE model differs from TP in that it better resolves the conducting continental crust layer (ρ = 14–46 Ω m) in a depth range of 25–45 km and the subvertical conducting zone (ρ = 12–46 Ω m) in a depth range of 45–110 km bounded by layers with resistivities of 147–1260 Ω m in the west and 215–612 Ω m in the east. One might say that the TE model is derived by modifying the TP model.

Note that if the START model is taken as a starting model, the $\varphi^{\parallel}$ inversion yields (independently of the TP model!) a model that contains the continental asthenosphere with a branching-out subvertical low-resistivity

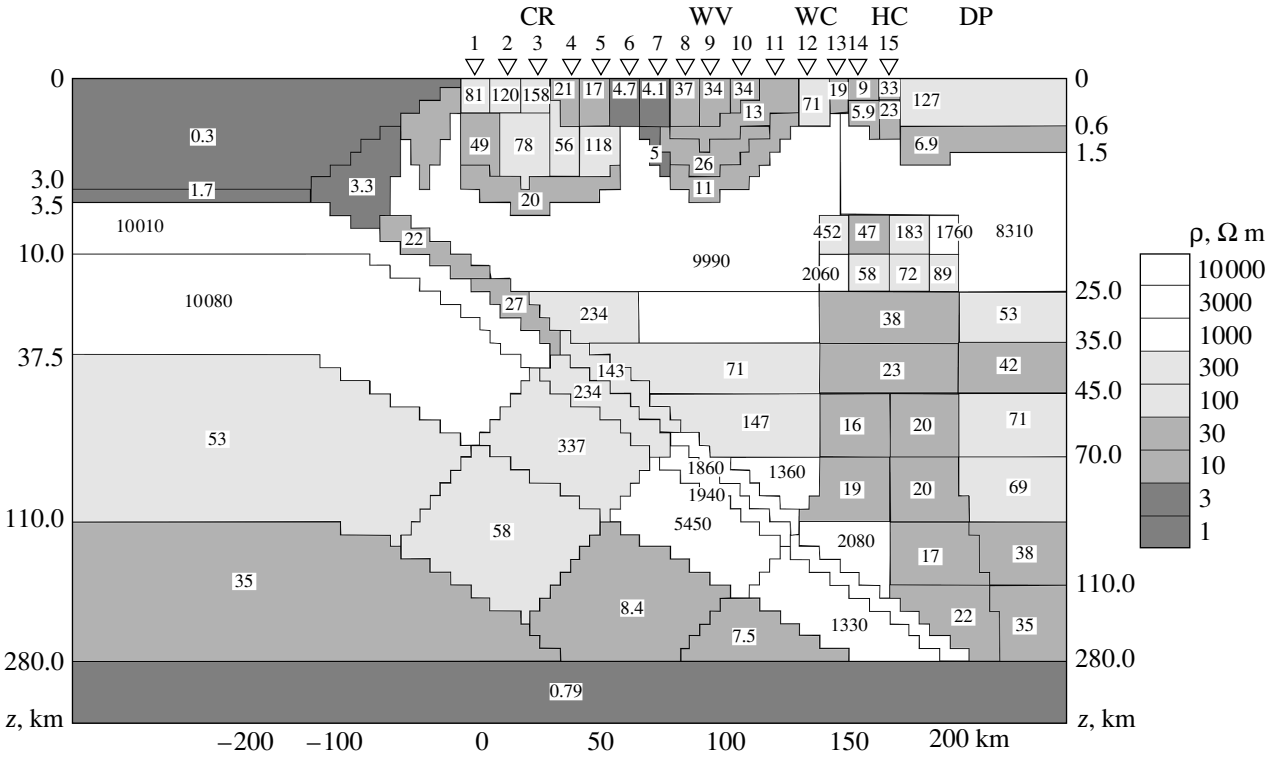

Fig. 23. TP model derived from the inversion of tippers. Notation is the same as in Fig. 21

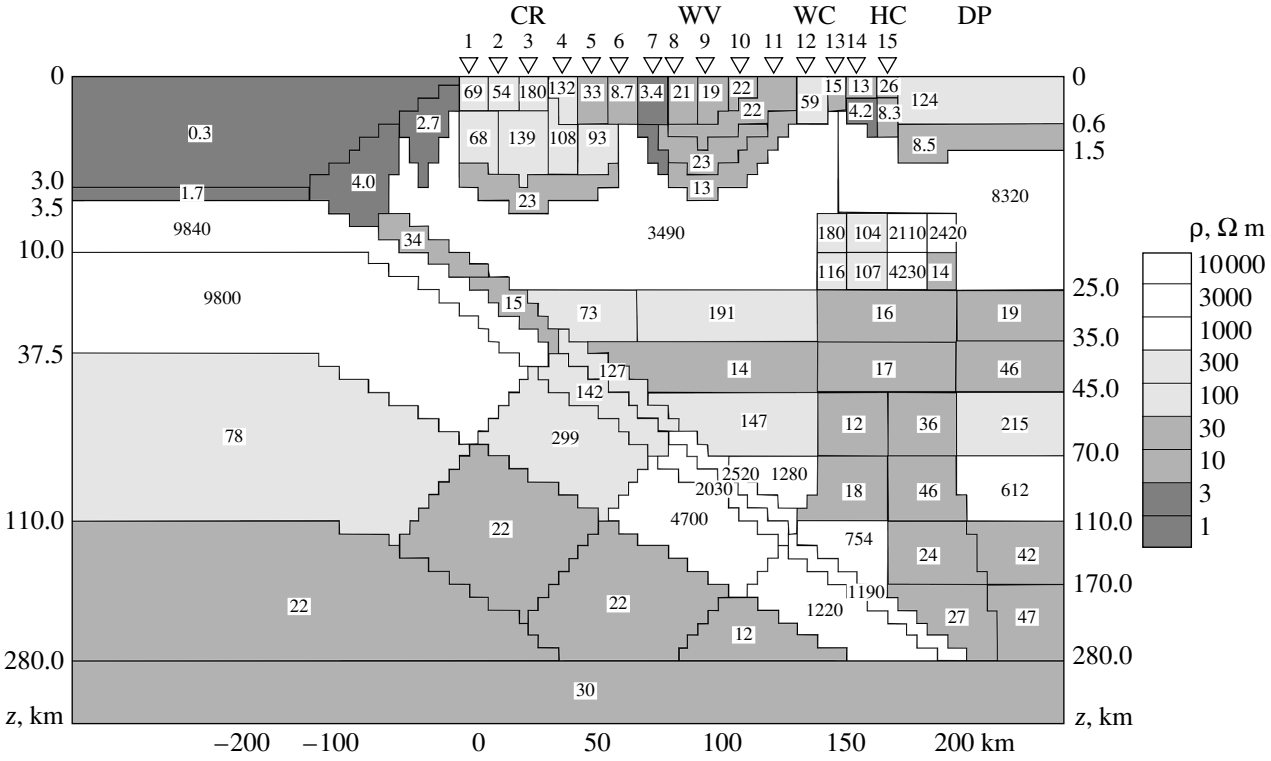

Fig. 24. TE model derived from the inversion of longitudinal impedance phases. Notation is the same as in Fig. 21.

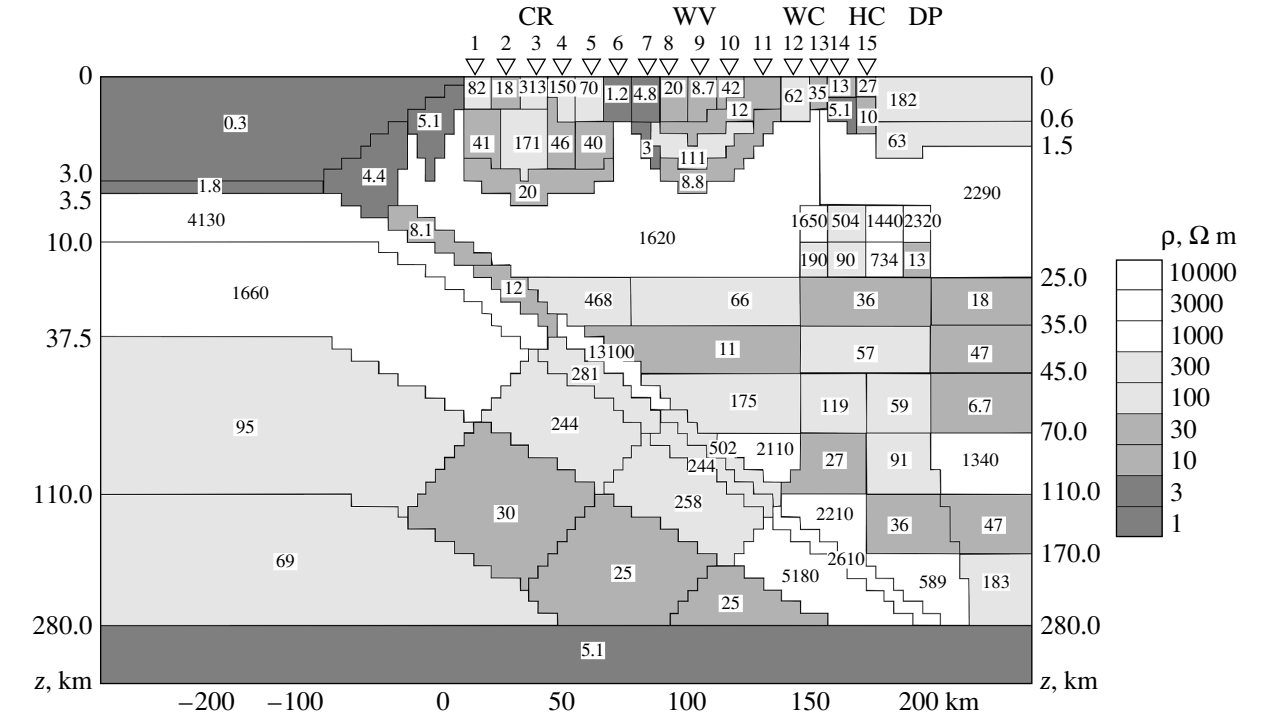

Fig. 25. TM model derived from the inversion of transverse resistivities and transverse impedance phases. Notation is the same as in Fig. 21.

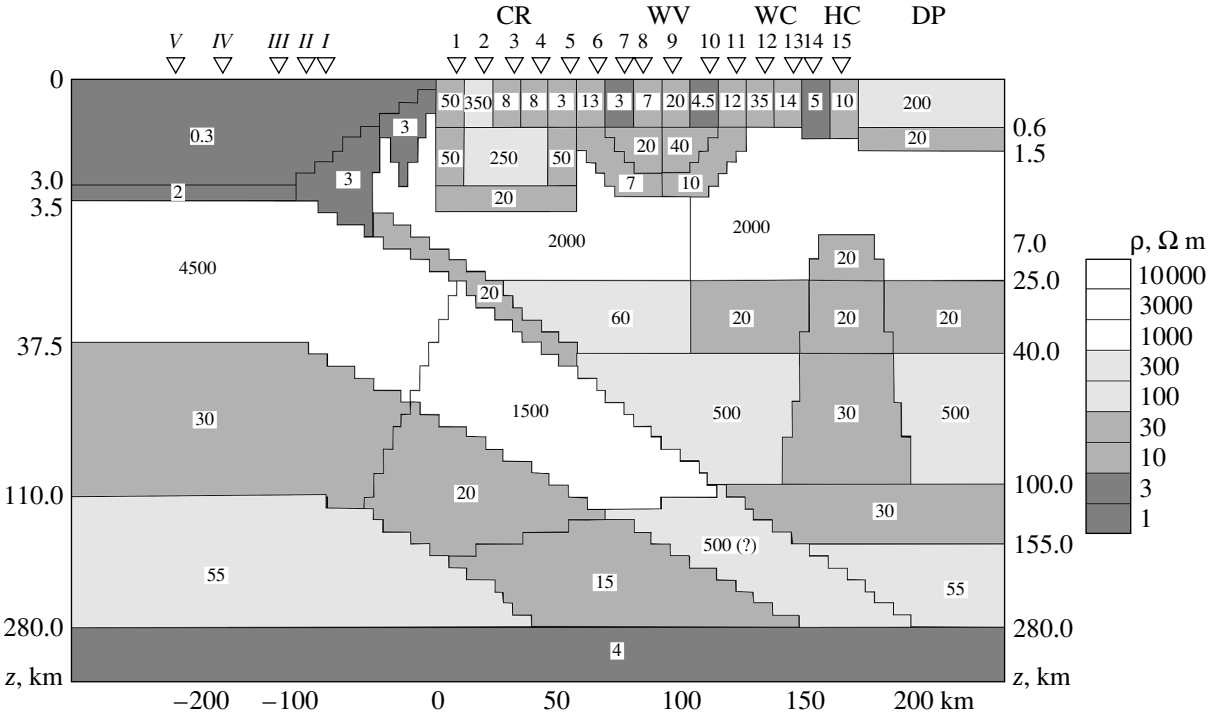

Fig. 26. EMSLAB III model. Notation is the same as in Fig. 21.

zone. Thus, the reliability of these structures is confirmed once again.

Level III: $\rho^{\perp}$ and $\varphi^{\perp}$ inversion. On this level, we address the TM mode, which is less sensitive to crustal and mantle conducting zones but more adequately images the juncture between the downgoing conducting plate and crustal conducting layer and provides better estimates of the resistivity of the upper solid crust. The starting model in the inversion of the TM mode is the TE model derived from the inversion of phases $\varphi^{\parallel}$.

The TM inversion residuals are given in Table 6, where $\delta\rho^{\perp}$ and $\delta\varphi^{\perp}$ are residuals of apparent resistivities and phases (rms deviations of the model results from the observed values) and $\Delta\varphi^{\perp} = |\max\varphi^{\perp} - \min\varphi^{\perp}|$ is the maximum variation in the observed phase values. The apparent resistivity residuals at most stations vary from 6 to 12%, and the phase residuals are 7 to 10 times smaller than the maximum phase variation. The inversion yielded the TM model shown in Fig. 25. It inherits the main features of the starting TE model (although with some deviations). What does the TM model indicate? First, a conductive juncture between the downgoing plate and crustal conducting layer is absent. Second, the upper solid continental crust has a resistivity of about 2000 Ω m.

Table 5. Residuals of $\varphi^{\parallel}$

Point	1	2	5	6	7	8	9	11	12	14	15
$\delta\varphi^{\parallel}$, deg	4.0	2.6	3.1	4.6	5.5	4.0	2.0	4.1	2.5	2.3	4.9
$\Delta\varphi^{\parallel}$, deg	23	21	21	23	45	38	29	42	20	29	41

Table 6. Residuals of $\rho^{\perp}$ and $\varphi^{\perp}$

Point	1	2	3	4	5	6	7	8	9	10	11	12	13	14	15
$\delta\rho^{\perp}$, %	12	12	11	10	18	16	13	11	18	7	6	11	12	12	9
$\delta\varphi^{\perp}$, deg	2.5	2.9	2.6	1.9	2.2	3.6	1.0	2.4	4.5	1.8	1.5	2.2	1.9	1.9	1.4
$\Delta\varphi^{\perp}$, deg	20	19	24	18	21	19	22	18	27	21	23	34	22	18	29

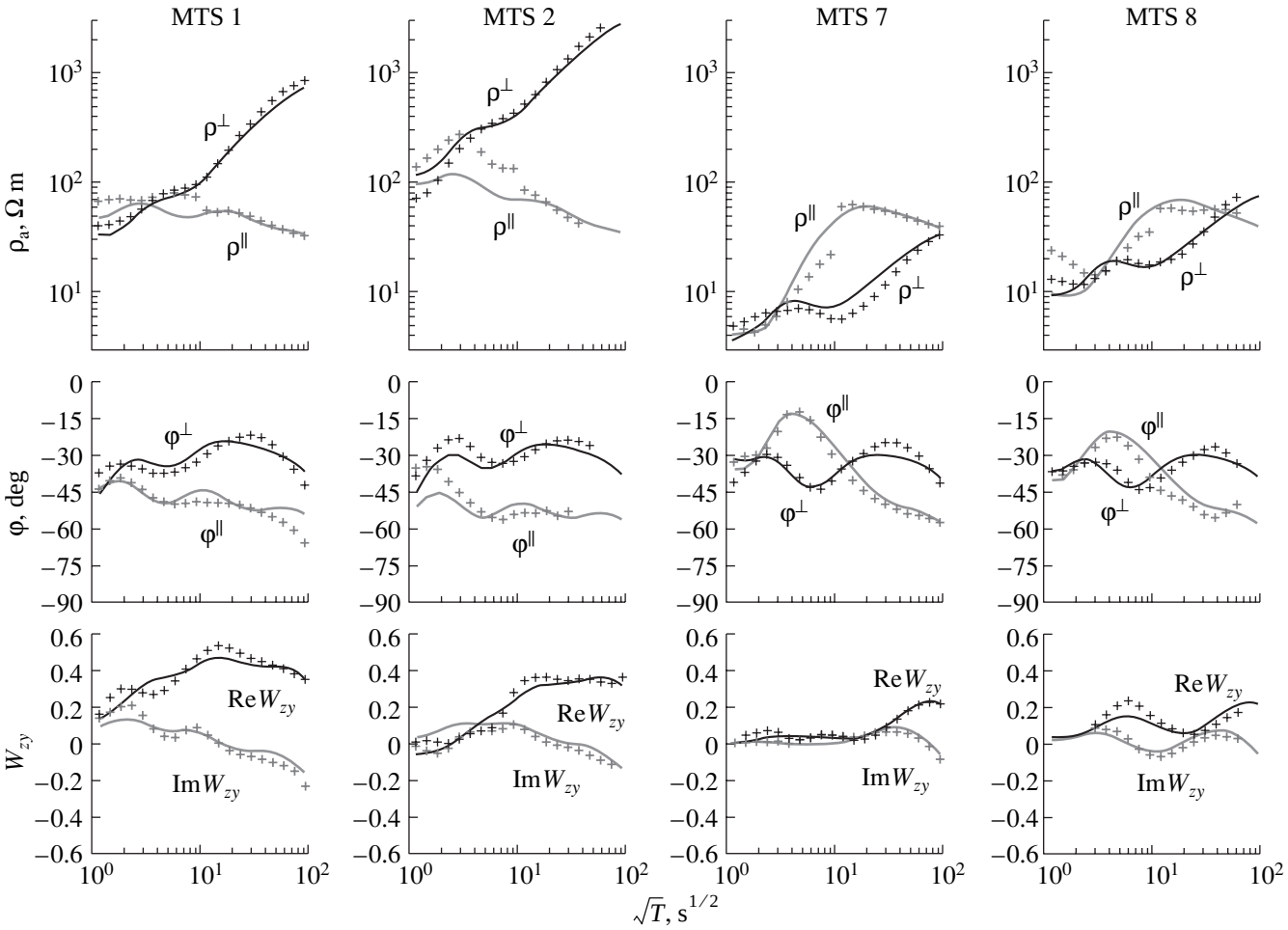

Fig. 27. Comparison of the observed MT and MV curves with the curves calculated from the EMSLAB III model: (*1*) observations; (*2*) EMSLAB III.

Note that the inversion of the TM mode essentially depends on the choice of the starting model. If the latter is the START model, the TM mode inversion yields a model devoid of the continental asthenosphere. This appears to be due to the low sensitivity of the TM mode to deep conducting structures. The underlying mechanism is here the same as that involved in the formation of the EMSLAB I model and described by Wannamaker *et al.* [1989b].

Level IV: generalization. On this level, we analyze the TP, TE, and TM models and construct the generalized model EMSLAB III, smoothing out inessential details and enlarging blocks. All changes were made in an interactive mode, with the calculation of local residuals and with the correction of shifted boundaries and averaged resistivities. The resulting generalized model is shown in Fig. 26. The amount of its agreement with the observed data can be assessed from Fig. 27, where the model curves $\rho^{\perp}$, $\rho^{\parallel}$, $\varphi^{\perp}$, $\varphi^{\parallel}$, $\mathrm{Re}\,W_{zy}$, and $\mathrm{Im}\,W_{zy}$ are compared with the observed curves (the static shift in the observed $\rho^{\parallel}$ curves is eliminated by a vertical displacement of their low-frequency branches).

CONCLUSION

The interpretation of MV and MT soundings on the Lincoln line resulted in the construction of a new model of the Cascadia subduction zone (EMSLAB III model).

In its oceanic part, the EMSLAB III model is similar to EMSLAB I and EMSLAB II, resolving a thick oceanic asthenosphere in a depth range of 37.5–110 km. The continental structure of the EMSLAB III model is distinguished by the following important features.

(1) A crustal conducting layer (ρ = 20 Ω m in a depth range of 25–40 km) and a conducting asthenosphere (ρ = 30 Ω m, 100–155 km) are clearly identifiable.

(2) The crustal and asthenosphere conductors are connected by a columnar conducting body (ρ = 20–30 Ω m) that penetrates through the lithosphere and reaches a depth of about 7 km under the volcanic zone of the High Cascades.

(3) The downgoing oceanic plate in a depth range of 4–40 km contains a thin inclined conductor (ρ = 20 Ω m) separated from the crustal conducting layer by a zone of higher resistivity (ρ = 60 Ω m); apparently, the crustal

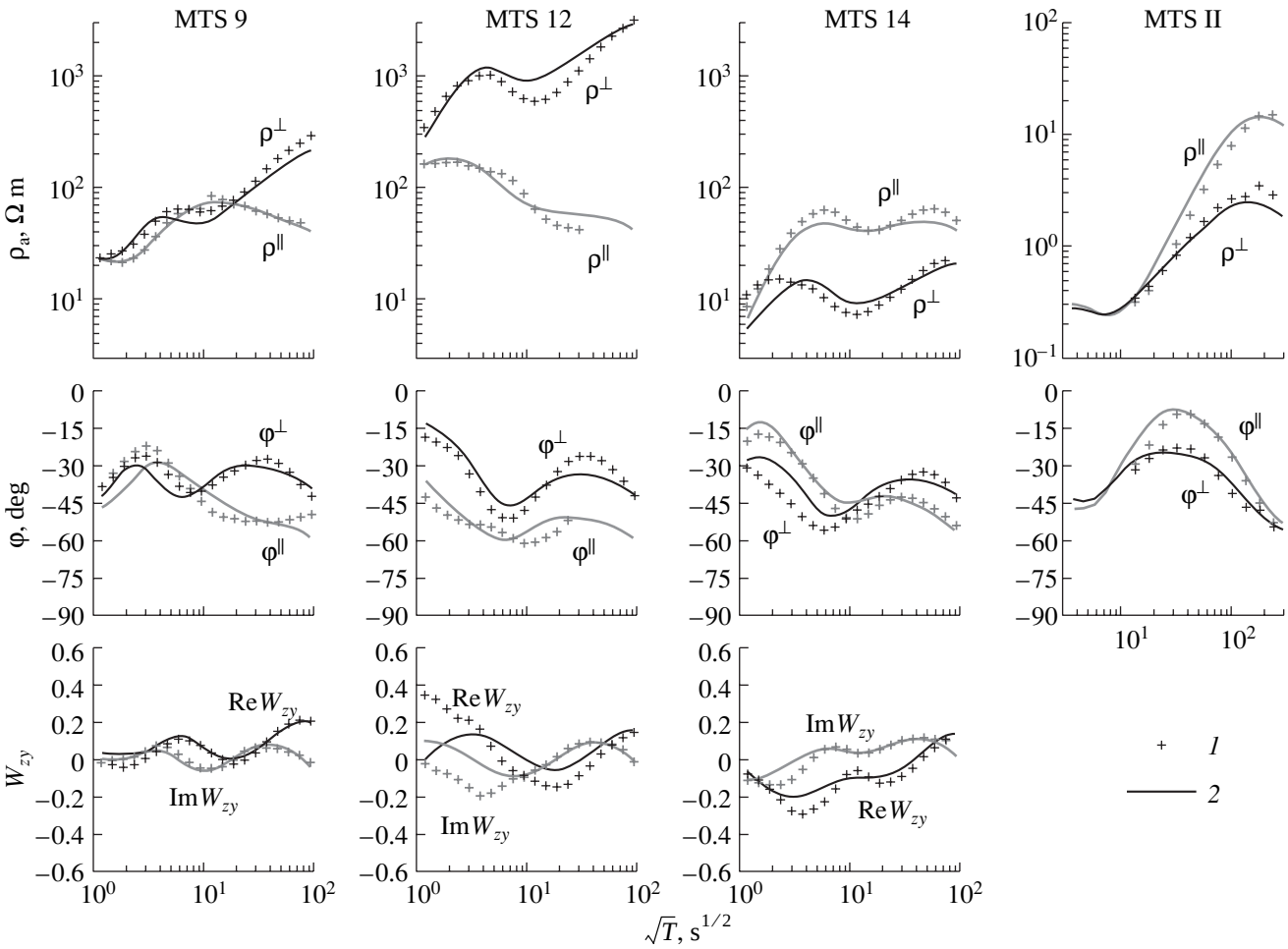

Fig. 27. (Contd.)

conducting layer is unrelated to the fluids of the subducting plate and has a deep origin.

These characteristics of the continental section make EMSLAB III similar to the predictive CASCADIA model. Here, the fluid regime of the subduction zone is clearly expressed. The downgoing plate drags low-resistivity water-saturated rocks of the ocean floor. The descent of the plate displaces free water, which migrates through the shear zone (at the contact between the subducting oceanic and stable continental plates). Dehydration (release of combined water), beginning at depths of about 30 to 40 km in the downgoing slab supplies fluids to the mantle and causes wet melting of asthenospheric material. Low-resistivity melts migrate upward through the lithosphere and form the volcanic arc. The heating of the lithosphere activates dehydration in the lower crust, forming the crustal conducting layer.

Thus, we confirm the validity of the hypotheses underpinning the CASCADIA model.

ACKNOWLEDGMENTS

We are grateful to A.F. Grachev, M.G. Lomize, V.I. Makarov, V.V. Spichak, V.I. Dmitriev, and I.M. Varentsov for discussions of results and useful comments. This work was supported by the Russian Foundation for Basic Research, project nos. 99-05-64758, 00-05-64660, and 02-05-64079.

REFERENCES

Bahr, K., Interpretation of Magnetotelluric Impedance Tensor: Regional Induction and Local Telluric Distortion, *J. Geophys.*, 1988, vol. 62, pp. 119–127.

Berdichevsky, M.N., Koldaev, D.S., and Yakovlev, A.G., MT Sounding on an Oceanic Coast, *Fiz. Zemli*, 1992, no. 6, pp. 87–96.

Berdichevsky, M.N. and Pokhotelov, D.O., Violation of Dispersion Relations in a 3-D MT Model, *Fiz. Zemli*, 1997, no. 8, pp. 3–12.

Berdichevsky, M.N., Dmitriev, V.I., Novikov, D.B., and Pastutsan, V.V., *Analiz i interpretatsiya magnitotellurichеskikh*

dannykh (Analysis and Interpretation of Magnetotelluric Data), Moscow: Dialog-MGU, 1997.

Berdichevsky, M.N., Dmitriev, V.I., and Mershchikova, N.A., *Ob obratnoi zadache zondirovaniya s ispol'zovaniem magnitotelluricheskikh i magnitovariatsionnykh dannykh* (Magnetotelluric and Magnetic Variation Sounding Data Inversion), Moscow: MAKS Press, 2000.

Blackwell, D.D., Steele, J.L., Frohne, M.K., *et al.*, Heat Flow in the Oregon Cascade Range and Its Correlation with Regional Gravity, Curie Point Depths, and Geology, *J. Geophys. Res.*, 1990, vol. 95, pp. 19475–19493.

Connard, G., Couch, R., Keeling, K., *et al.*, Abyssal Plain and Continental Net-Objective Sedimentary Thickness, *Western North American Continental Margin and Adjacent Ocean Floor off Oregon and Washington, Atlas 1. Ocean Margin Drilling Program*, L.D. Kulm *et al.*, Eds., 1984a (Regional Atlas Series: Marine Science International, sheet 7).

Connard, G., Couch, R., Pitts, G.S., and Troseth, S., Bathymetry and Topography, *Western North American Continental Margin and Adjacent Ocean Floor off Oregon and Washington, Atlas 1. Ocean Margin Drilling Program*, L.D. Kulm *et al.*, Eds., 1984b (Regional Atlas Series: Marine Science International, sheet 1).

Golubev, N.G. and Varentsov, I.M., TM-Data Inversion: Stable Optimization Methods and Interactive Graphics, *Abstracts of XII Workshop on EM Induction in the Earth*, 1994.

Ingebritsen, S.E., Sherrod, D.R., and Mariner, R.H., Heat Flow and Hydrothermal Circulation in the Cascade Range, North-Central Oregon, *Science*, 1989, vol. 243, pp. 1458–1462.

Jiracek, G.R., Curtis, J.H., Ramirez, J., *et al.*, Two-Dimensional Magnetotelluric Inversion of the EMSLAB Lincoln Line, *J. Geophys. Res.*, 1989, vol. 94, pp. 14145–14151.

Kelly, S.M. and Crosson, R.S., Historical Seismicity 1841–1979. Seismicity 1970–1979, *Western North American Continental Margin and Adjacent Ocean Floor off Oregon and Washington, Atlas 1. Ocean Margin Drilling Program*, L.D. Kulm *et al.*, Eds., 1984 (Regional Atlas Series: Marine Science International, sheets 10–11).

Khain, V., Leonov, Yu., and Dottin, O., Eds., *Tectonics of Continents and Oceans. Explanatory Note to the International Tectonic Map of the World, Scale 1 : 500000*, Moscow: Nauka, 1988.

Khain, V.E. and Lomize, M.G., *Geotektonika s osnovami geodinamiki* (Geotectonics with Fundamentals of Geodynamics), Moscow: MGU, 1995.

Novozhinskii, K. and Pushkarev, P.Yu., The Efficiency Analysis of Programs for Two-Dimensional Inversion of Magnetotelluric Data, *Izvestiya, Phys. Solid Earth*, 2001, vol. 37, pp. 503–516.

Palshin, N.A., Vanyan, L.L., Egorov, I.V., and Lebedev, K.N., Electric Fields Induced by the Global Ocean Circulation, *Izvestiya, Phys. Solid Earth*, 1999, vol. 35, pp. 1028–1035.

Ramires, J.H., *Modelato Bidimensional del Perfil Magnetotellurico de EMSLAB-Juan de Fuca*, CICESE, Dissertation, 1988.

Rasmussen, J. and Humphries, G., Tomographic Image of the Juan de Fuca Plate beneath Washington and Western Oregon Using Teleseismic *P*-Wave Travel Times, *Geophys. Res. Lett.*, 1988, no. 15, pp. 1417–1420.

Romanyuk, T.V., Mooney, W.D., and Blakely, R.J., Density Model of the Cascadia Subduction Zone, *Izvestiya, Phys. Solid Earth*, 2001a, vol. 8, pp. 3–22.

Romanyuk, T.V., Mooney, V.D., and Blakely, R.J., Tectonic–Geophysical Model of the Cascadia Subduction Zone, North America, *Geotektonika*, no. 3, pp. 88–110.

Singer, B.Sh. and Fainberg, E.B., *Elektromagnitnaya induktsiya v neodnorodnykh tonkikh sloyakh* (Electromagnetic Induction in Heterogeneous Thin Layers), Moscow: IZMIRAN, 1985.

Singer, B.Sh. and Fainberg, E.B., Generalization of the Iterative Dissipative Method for Modeling Electromagnetic Fields in Nonuniform Media with Displacement Currents, *Appl. Geophys.*, 1995, vol. 34, pp. 41–46.

Siripunvaraporn, W. and Egbert, G., An Efficient Data-Subspace Inversion Method for 2-D Magnetotelluric Data, *Geophysics*, vol. 65, pp. 791–803.

Spichak, V.V., *Magnitotelluricheskie polya v trekhmernykh modelyakh geoelektriki* (Magnetotelluric Fields in Three-Dimensional Geoelectric Models), Moscow: Nauchnyi Mir, 1999.

Stanley, D.W., Tectonic Study of Cascade Range and Columbia upon Magnetotelluric Sounding, *J. Geophys. Res.*, 1984, vol. 89, pp. 4447–4460.

Stanley, W.D., Fuis, G.S., and Mooney, W.D., Details of Crustal Structure in the Cascade Range and Surrounding Region from Seismic and Magnetotelluric Data, in Geological, Geophysical and Tectonic Setting of the Cascades Range, *Open File Rep. 89–178*, U.S. Geol. Surv., 1989, pp. 31–73.

Swift, C.M., A Magnetotelluric Investigation of an Electrical Conductivity Anomaly in the Southwestern United States, *Dissertation, MIT*, 1967, Cambridge.

Trehu, A.M., Asudeh, I., Brocher, T.M., *et al.*, Crustal Architecture of the Cascadia Forearc, *Science*, 1994, vol. 265, pp. 237–243.

Vanyan, L.L., *Elektromagnitnye zondirovaniya* (Electromagnetic Sounding Studies), Moscow: Nauchnyi Mir, 1997.

Vanyan, L., Palshin, N., Poray-Koshits, A., *et al.*, The Preliminary Interpretation of the EMSLAB MT-Soundings, *Abstracts of IX Workshop on EM induction in the Earth*, 1988.

Varentsov, I.M., Stable Nonlinear Inversion of Magnetotelluric Data in the Piecewise Continuous 3D Media. Three-Dimensional Electromagnetics (3DEM-2), *Proc. 3DEM-2 Int. Symp.*, M. Oristaglio and B. Spies, Eds., Salt Lake City: Univ. of Utah, 1999.

Varentsov, I.M., A General Approach to the Magnetotelluric Data Inversion in a Piecewise-Continuous Medium, *Izvestiya, Phys. Solid Earth*, 2002, vol. 38 (in press).

Varentsov, Iv.M., Golubev, N.G., Gordienko. V.V., and Sokolova, E.Yu., Study of the Deep Geoelectric Structure along the Lincoln Line (EMSLAB Experiment), *Fiz. Zemli*, 1996, no. 4, pp. 124–144.

Wannamaker, P.E., Booker, J.R., Filloux, J.H., *et al.*, Magnetotelluric Observations across the Juan de Fuca Subduction System in the EMSLAB Project, *J. Geophys. Res.*, 1989a, vol. 94, pp. 14111–14125.

Wannamaker, P.E., Booker, J.R., Jones, A.G., *et al.*, Resistivity Cross Section through the Juan de Fuca Subduction System and Its Tectonic Implications, *J. Geophys. Res.*, 1989, vol. 94, pp. 14127–14144.

Weaver, C.S. and Michaelson, C.A., Seismicity and Volcanism in the Pacific Northwest: Evidence for the Segmentation of the Juan de Fuca Plate, *Geophys. Res. Lett.*, 1985, vol. 12, pp. 215–218.

Zhdanov, M.S. and Spichak, V.V., *Matematicheskoe modelirovanie elektromagnitnykh polei v trekhmerno-neodnorodnykh sredakh* (Mathematical Simulation of Electromagnetic Fields in Three-Dimensional Heterogeneous Media), Moscow: Nauka, 1992.